A Computational Study of the Hydrodynamics of Gas-Solid Fluidized Beds

Lindsey Teaters

Thesis submitted to the faculty of the Virginia Polytechnic Institute and State University in partial fulfillment of the requirements for the degree of

Master of Science

In

Mechanical Engineering

Francine Battaglia
Javid Bayandor
Brian Y Lattimer

May 31, 2012

Blacksburg, VA

Keywords: Fluidized beds; pressure drop; minimum fluidization velocity

A Computational Study of the Hydrodynamics of Gas-Solid Fluidized Beds

Lindsey Teaters

ABSTRACT

Computational fluid dynamics (CFD) modeling was used to predict the gas-solid hydrodynamics of fluidized beds. An Eulerian-Eulerian multi-fluid model and granular kinetic theory were used to simulate fluidization and to capture the complex physics associated therewith. The commercial code ANSYS FLUENT was used to study two-dimensional single solids phase glass bead and walnut shell fluidized beds. Current modeling codes only allow for modeling of spherical, uniform-density particles. Owing to the fact that biomass material, such as walnut shell, is abnormally shaped and has non-uniform density, a study was conducted to find the best modeling approach to accurately predict pressure drop, minimum fluidization velocity, and void fraction in the bed. Furthermore, experiments have revealed that all of the bed mass does not completely fluidize due to agglomeration of material between jets in the distributor plate. It was shown that the best modeling approach to capture the physics of the biomass bed was by correcting the amount of mass present in the bed in order to match how much material truly fluidizes experimentally, whereby the initial bed height of the system is altered. The approach was referred to as the SIM approach. A flow regime identification study was also performed on a glass bead fluidized bed to show the distinction between bubbling, slugging, and turbulent flow regimes by examining void fraction contours and bubble dynamics, as well as by comparison of simulated data with an established trend of standard deviation of pressure versus inlet gas velocity. Modeling was carried out with and without turbulence modeling ($k-\epsilon$), to show the effect of turbulence modeling on two-dimensional simulations.

Acknowledgements

There are a great deal of people to whom I owe gratitude for successful completion of my Master's degree. To begin, I would like to thank my graduate advisor, Dr. Francine Battaglia, for her guidance, support , and constant knack for finding time to lend a helping hand despite a busy schedule. I would like to thank Dr. Javid Bayandor and Dr. Brian Lattimer for offering to serve as my committee members and for taking time to get to know my research. Without a doubt, I must thank my fellow graduate students in the CREST lab for helping me out whenever I had any issue without question. Finally, I must thank my parents, who encouraged me to return to school and supported me whole-heartedly over the last two years.

Table of Contents

Acknowledgements iii
Table of Figures vi
Table of Tables ix
Nomenclature x
Chapter 1 Introduction 1
1.1 Purpose and Applications 1
1.2 Objectives 2
1.3 Outline of the Thesis 3
Chapter 2 Background Theory and Literature Review 4
2.1 Reactor Design 4
2.2 Pressure Drop and Minimum Fluidization Velocity 6
2.3 Drag Modeling Comparisons 9
2.4 Particle Characterization 11
2.5 Fluidization Regimes 11
2.6 Modeling Platforms 12
Chapter 3 Methodology 15
3.1 Governing Equations 15
3.1.1 Conservation of Mass 16
3.1.2 Conservation of Momentum 16
3.1.3 Granular Temperature 20
3.2 Numerical Approach 21
3.2.1 Pressure-Based Solver Algorithm 21
3.2.2 Spatial Discretization 22
3.2.3 Initial and Boundary Conditions 23
Chapter 4 Grid Resolution Study 26
4.1 Experimental Setup and Procedure 26
4.2 Computational Setup and Bed Parameters 27
4.3 Grid Resolutions and Case Results 29
Chapter 5 Modeling Approach Comparison 37
5.1 Alternative Drag Model 37
5.2 Modeling Approaches: STD, NEW, and SIM 38

5.3 Void Fraction Results and Discussion 40
5.4 Pressure Drop Results and Discussion 44
Chapter 6 Flow Regime Characterization 47
6.1 Pressure Fluctuation Analysis 47
6.1.1 Standard Deviation 47
6.1.2 Frequency Analysis 48
6.2 Turbulence Modeling 49
6.3 Problem Setup 50
6.4 Numerical Results and Discussion 52
Chapter 7 Conclusions and Future Work 62
Bibliography 64

Table of Figures

Figure 2.1 Fluidized bed reactor geometry 5

Figure 2.2 Force balance on bed material 6

Figure 2.3 Relationship between pressure drop and inlet gas velocity 7

Figure 2.4 Fluidization regimes for fluidized beds [Image reprinted with permission (Deza 2012)] 12

Figure 3.1 One-dimensional control volume used in QUICK scheme 21

Figure 3.2 Example of no slip wall boundary condition 24

Figure 4.1 Schematic of the primary portion of the fluidized bed for the grid resolution study [Image reprinted with permission (Deza 2012)] 28

Figure 4.2 Instantaneous void fraction contours for a flow time of 20 seconds for each of the grid resolutions (a)-(d) 30

Figure 4.3 Time-averaged void fraction profiles of simulation data for each different grid resolution at (a) z = 4 cm and (b) z=8 cm 31

Figure 4.4 Instantaneous void fraction contours for the glass bead fluidized bed. Images are displayed in a time progression from (a) 10 s, (b) 20 s, (c) 30 s, and (d) 40 s 32

Figure 4.5 Time-averaged void fraction contours of the glass bead bed of the simulated cases (a)-(d) 33

Figure 4.6 Time-averaged void fraction profiles comparing glass bead simulations with experimental data at (a) z = 4 cm and (b) z = 8 cm 35

Figure 4.7 Bed height versus time- and plane-averaged void fraction for each grid resolution and experimental data 36

Figure 5.1 Time-averaged void fraction profiles comparing walnut shell bed simulations with experimental data at (a) h/h_0=0.25, (b) h/h_0=0.5, (c) h/h_0=0.75, and (d) h/h_0=1 41

Figure 5.2 Time- and plane-averaged void fraction versus bed height normalized with bed diameter for the walnut shell fluidized bed..... 42
Figure 5.3 Time- and plane-averaged void fraction versus bed height normalized with bed diameter for the walnut shell fluidized bed..... 42
Figure 5.4 Plot of pressure drop versus inlet gas velocity for the walnut shell fluidized bed for simulations having 'Case 1' parameters from Table 5.2..... 43
Figure 5.5 Plot of pressure drop versus inlet gas velocity for the walnut shell fluidized bed of the SIM approach parametric study. 45
Figure 6.1 Flow regime characterization based on plot of standard deviation versus inlet gas velocity [Image reprinted with permission (Deza 2012)] 48
Figure 6.2 Pressure fluctuations vs. flow time for the glass bead fluidized bed operating at an inlet gas velocity of 2 Umf for (a) no turbulence model and (b) k-epsilon turbulence model 51
Figure 6.3 Standard deviation of pressure versus inlet gas velocity for simulations with and without a turbulence model..... 52
Figure 6.4 Standard deviation of pressure versus inlet gas velocity combining the best results of simulations including and excluding a turbulence model..... 53
Figure 6.5 Instantaneous void fraction contours of the glass bead fluidized bed without a turbulence model at five sequential flow times for inlet gas velocities of 3 Umf (top), 5 Umf (middle), and 7 Umf (bottom) 55
Figure 6.6 Instantaneous void fraction contours of the glass bead fluidized bed with the $k-\epsilon$ turbulence model at five sequential flow times for inlet gas velocities of 3 Umf (top), 5 Umf (middle), and 7 Umf (bottom) 56

Figure 6.7 Pairs of time-averaged void fraction contours for inlet gas velocities (a) 3 Umf, (b) 5 Umf, and (c) 7 Umf for no turbulence model (left) and $k-\epsilon$ turbulence model (right)..... 58
Figure 6.8 Pairs of instantaneous void fraction (left) and velocity vectors (right) for the glass bead fluidized bed without turbulence modeling for inlet gas velocities (a) 3 Umf, (b) 5 Umf, and (c) 7 Umf at approximately 10 s flow time..... 59
Figure 6.9 Time- and plane-averaged void fraction versus bed height for the glass bead fluidized bed at various inlet gas velocities 60

Table of Tables

Table 2.1 Drag model correlations..... 10

Table 4.1 Glass bead bed properties 28

Table 4.2 Grid resolution parameters..... 29

Table 5.1 Walnut shell bed properties 40

Table 5.2 Pressure drop parametric study case parameter.....44

Nomenclature

A	cross-sectional area
Ar	Archimedes number
C_D	drag coefficient
d_s	particle diameter
D	diameter
g	acceleration of gravity
$g_{0,ss}$	radial distribution term
G_k	turbulent kinetic energy
H	total reactor height
h_0	static bed height
$\bar{\bar{I}}$	identity matrix
k_{Θ_s}	diffusion coefficient
K	interphase momentum exchange coefficient
m	mass
p	pressure
Q	gas volumetric flow rate
R	interaction force
Re	Reynolds number
S	mass source term
U	inlet gas velocity
$v_{r,s}$	terminal particle velocity
$\forall$	volume
ΔP	pressure drop
ε	volume fraction
Θ	granular temperature
λ	bulk viscosity
μ	shear viscosity
ρ	density
σ	standard deviation of pressure
$\bar{\bar{\tau}}$	stress tensor
τ_s	particle relaxation time
φ	energy exchange
ϕ	scalar quantity
ψ	sphericity

Subscripts/Superscripts

b	bulk
g	gas phase
m	mixture
mf	minimum fluidization
p	particle
s	solids phase

Chapter 1 Introduction

1.1 Purpose and Applications

Fluidized beds have various industrial uses ranging from fluid catalytic cracking, combustion, gasification, and pyrolysis, to coating processes used in the pharmaceutical industry [1-6]. Most notably, the recent demand for cleaner, sustainable energy has boosted biomass applications to the forefront of possible solutions. Biomass feedstock is available in many forms including wood chips, straw, corn stalks, animal waste, or any other waste organic material. It is clear from the types of feedstock mentioned that these do not constitute conventional combustible material. The shape, water contents, and often low heating values make these materials poor candidates for conventional combustion: this is where fluidized bed technology comes into play [4].

Fluidized bed combustion offer several advantages over conventional combustion technologies including better heat transfer characteristics due to uniform particle mixing, lower temperature requirements, near isothermal process conditions, and continuous operation ability [1]. Biomass can also be processed using fluidized beds through gasification and pyrolysis [2]. Gasification occurs when the biomass feedstock is heated in an oxygen-starved environment to create gas, solid, and liquid by-products. Pyrolysis is similar to gasification, only the process occurs in an oxygen-free environment and typically at lower temperatures than required for gasification. The main desired product of gasification and pyrolysis is synthetic gas (syngas), which is a gaseous mixture composed primarily of carbon monoxide (CO) and hydrogen (H_2). Syngas can be used directly as a fuel or as a chemical feedstock in the oil refining industries.

The process of fluidization can be described simply as supplying a flow of gas through a bed of granular material at a sufficient velocity such that the granular bed behaves as a fluid [3]. The actual physics behind fluidization that constitute the crux of the present work, however, are not so simple. Fluidization of biomass material is still a fairly new topic of interest; as such, the characteristics of biomass fluidization are relatively unexplored. It is critical for efficient biomass combustion, gasification, and pyrolysis, to be able to understand and predict important fluidization aspects such as pressure drop and minimum fluidization velocity. There are two sides of study currently employed in fluidized bed research: experiments and computational validation studies. Experimental studies are conducted on small-scale fluidized beds and computational fluid dynamics (CFD) codes are used to model existing experimental setups and validate the experimental results. If CFD models can be shown to recreate experimental data accurately, then these models can be used to design large-scale fluidized bed facilities without prior physical testing.

1.2 Objectives

The main objective of the present work is to use the commercial CFD code ANSYS FLUENT v12.0 to model fluidized bed behavior and compare modeling results from FLUENT to experimental data as well as data from an alternative CFD code, Multiphase Flow with Interphase eXchange (MFIX). FLUENT is a comprehensive commercial code which does not focus solely on multiphase flows, while MFIX is specific for fluidized bed reactor modeling and design. It is further desired to use these comparisons to establish the strengths and limitations of using FLUENT to model multiphase flow. More specifically, present work will examine the validity of using FLUENT to model fluidized beds in the unfluidized bed regime versus the fluidized bed regime through pressure drop and phasic volume fraction studies. Another aim of

the present work is to perform flow regime modeling and confirm that FLUENT provides results consistent with each flow regime (bubbling, slugging, and turbulent) for the expected corresponding inlet gas velocities. From the objectives outlined herein, the intended purpose of the present work is to enhance understanding of using FLUENT to model fluidized beds. Even more so, to find the best approach to model fluidized beds with limited experimental information as it is challenging to trust simulations where full geometry of the reactor is not modeled.

1.3 Outline of the Thesis

Chapter 2 provides an overview of fluidization background theory including discussions of pressure drop, minimum fluidization velocity, and distinguishing between flow regimes. The chapter also gives a review of relevant fluidization work. Chapter 3 presents the methodology behind modeling fluidized beds including the governing equations and numerical approaches employed by FLUENT v12.0. Chapter 4 details a grid resolution study using a glass bead fluidized bed. Chapter 5 examines a pressure drop study between unfluidized and fluidized bed regimes for a biomass fluidized bed using three approaches based on suggestions in the literature. Chapter 6 provides a flow regime characterization study using pressure fluctuation analysis of a glass bead fluidized bed. Chapter 7 is a summary of conclusions drawn from the research presented in chapters 4, 5, and 6, as well as suggested future work.

Chapter 2 Background Theory and Literature Review

The following chapter provides insight into fluidized bed reactor design, basic fluidization theory, and experimental setups. Chapter 2 also serves to highlight existing relevant work.

2.1 Reactor Design

While imaginably many different configurations of fluidized bed reactors exist, some having complex geometries, reactors can most generally be thought of as having a cylindrical geometry. Figure 2.1 depicts the primary section of a fluidized bed reactor having an internal diameter, *D* and a total height, *H*, the product of these two dimensions giving the area of the center-plane of the reactor. The reactor has an air inlet hose and distributor (not shown) located below the gas plenum. The gas plenum region serves to create a constant pressure distribution. A distributor plate located directly above the gas plenum serves to produce a near uniform flow of gas to be passed through the granular bed. The flow of gas through the granular bed is the mechanism by which fluidization is achieved. The bed of granular material has an initial height, h_0. The area directly above the granular bed is the freeboard which is characterized by having only gas phase. The outlet condition of a fluidized bed reactor is dependent on reactor design. Experimental fluidized beds, however, typically have outlets open to the atmosphere.

Superficial gas velocity, U_g, is defined as the velocity of the gas through the granular bed taking into account the reduced cross-sectional area due to the presence of the granular material. Directly above the distributor plate, as mentioned previously, the gas flow is assumed to be uniform, and the volume fraction of granular solids is assumed to be zero since reactors generally include a mesh screen located above the distributor plate to prevent backflow of bed material.

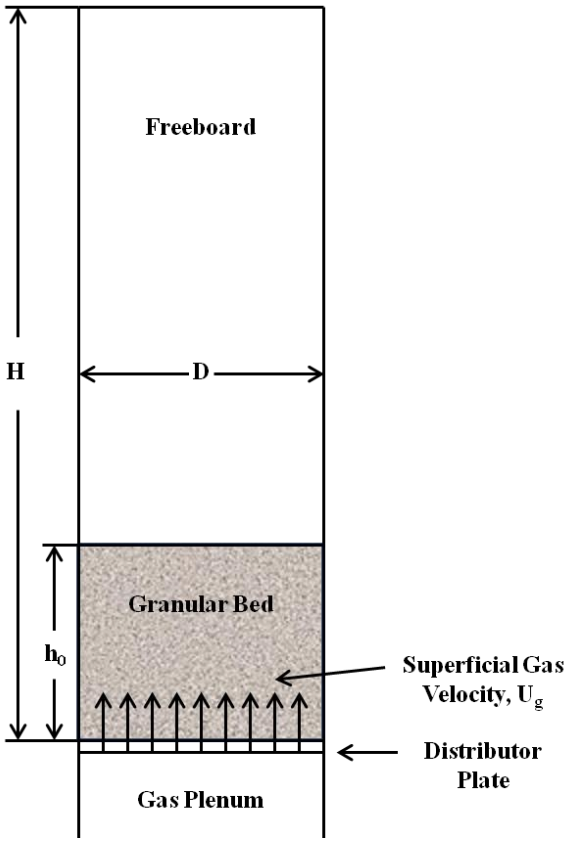

Figure 2.1 Fluidized bed reactor geometry

Since a uniform gas flow profile is assumed, the distributor plate is not generally modeled. Therefore, the superficial inlet gas velocity can be calculated using:

$$U_g = \frac{Q}{A} \qquad 2.1$$

where A is the circular cross-sectional area of the cylindrical reactor and Q is the volumetric flow rate in the gas plenum region. Accordingly, the superficial inlet gas velocity is also the value used to specify the inlet gas velocity boundary condition.

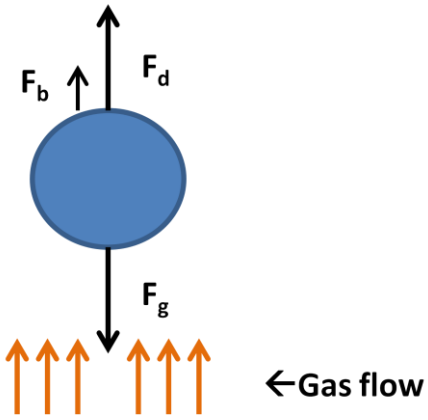

Figure 2.2 Force balance on bed material

2.2 Pressure Drop and Minimum Fluidization Velocity

The most fundamental characteristic studied in fluidized beds is the relationship between pressure drop across the bed and inlet gas velocity (superficial gas velocity at the inlet) [3]. Flowing gas upward through the bed of granular material creates a drag force, F_d, and a buoyancy force, F_b, on the particles. As the gas velocity is increased, the drag force increases, which in turn increases pressure drop, ΔP. At a certain inlet gas velocity the drag and buoyancy forces on the granular material balance the gravitational force, F_g, or weight of the bed, and the bed becomes fluidized. Figure 2.2 shows the forces acting on the granular bed material. When the bed becomes fluidized, the pressure drop across the bed remains a constant value, ΔP_{bed}, regardless of further increases in the inlet gas velocity, as shown in Figure 2.3. The inlet gas velocity corresponding to the moment of fluidization is known commonly as the minimum fluidization velocity, U_{mf}.

Minimum fluidization velocity and pressure drop are key for characterizing and understanding operation and design of fluidized beds. Pressure drop can be ascertained through experiments or established correlations. Total pressure drop across the bed can be expressed as:

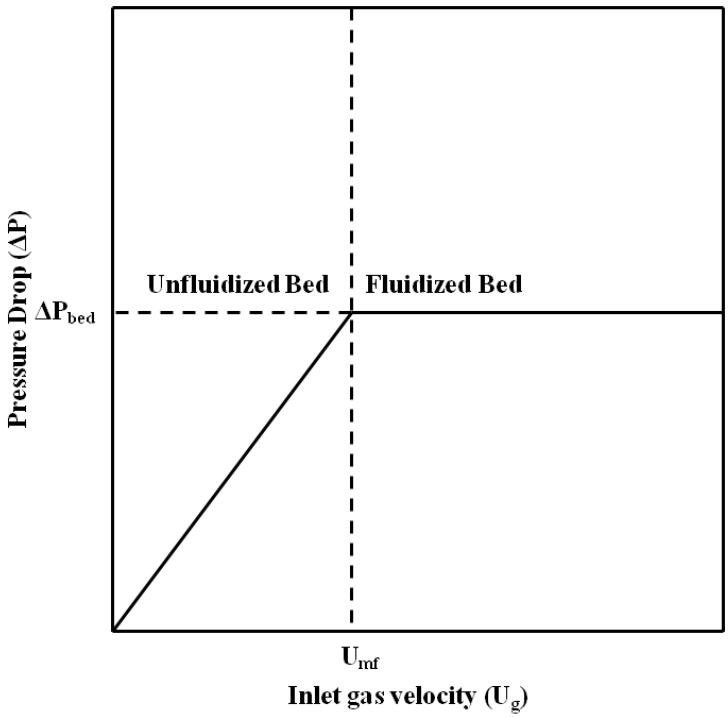

Figure 2.3 Relationship between pressure drop and inlet gas velocity

$$\Delta P_{bed} = \frac{mg}{A} \qquad 2.2$$

where m is the mass of the granular bed material, g is gravity, and A is the cross-sectional area of the bed. Alternatively, for a fixed bed, the mass can be expressed in terms of a bulk density, ρ_b, and an initial volume, V_0. The bulk density is defined assuming that the density of the gaseous phase is negligible compared to the density of the solids phase granular material. Bulk density is given by:

$$\rho_b = \varepsilon_s \rho_s \qquad 2.3$$

where ε_s is the solids volume fraction and ρ_s is the solids density. The mass of the bed can therefore be represented as:

$$m = \rho_b \forall_0 \tag{2.4}$$

Substituting Equation 2.4 into Equation 2.2 and noting that $\forall_0 = Ah_0$, the pressure drop is:

$$\Delta P_{bed} = \rho_b g h_0 \tag{2.5}$$

where h_0 is the initial height of the granular bed.

The Ergun correlation [7] is used to predict minimum fluidization velocity, U_{mf}, for a fluidized bed having a single solids phase. The Ergun correlation is expressed as:

$$\frac{1.75}{\psi_s \varepsilon_{mf,g}^3} Re_{mf}^2 + \frac{150\left(1-\varepsilon_{mf,g}\right)}{\psi_s^2 \varepsilon_{mf,g}^3} Re_{mf} = Ar \tag{2.6}$$

where $\varepsilon_{mf,g}$ is the volume fraction of the gas (void fraction) at fluidization, ψ_s is the solids sphericity, Re_{mf} is the Reynolds number at fluidization given by:

$$Re_{mf} = \frac{\rho_g d_s U_{mf}}{\mu_g} \tag{2.7}$$

and Ar is the Archimedes number given by:

$$Ar = \frac{\rho_g d_s^3 \left(\rho_s - \rho_g\right) g}{\mu_g^2} \tag{2.8}$$

where ρ_g is the gas density, d_s is the solids diameter, and μ_g is the gas viscosity. Assuming that the drag force balances the buoyancy and gravity forces on a particle at minimum fluidization, the following relationship for U_{mf} can be attained:

$$U_{mf} = \frac{(d_s \psi_s)^2 \left(\rho_s - \rho_g\right) g}{150 \mu_g} \cdot \frac{\varepsilon_{mf,g}^3}{1-\varepsilon_{mf,g}} \tag{2.9}$$

for $Re_{mf} < 20$.

2.3 Drag Modeling Comparisons

Various drag models have been suggested in the literature for predicting gas-solid flow interactions. Several studies have been conducted based on the suggested drag models in order to identify which models most accurately predict, qualitatively and quantitatively, fluidized bed hydrodynamics.

One of such studies, performed by Taghipour et al. [8], compared the Syamlal-O'Brien [9], Gidaspow [3], and Wen-Yu [10] models with experimental data. Each of the models showed reasonable agreement with experimental data through flow contours and void fraction profiles. Du et al. [11] compared the effects of the Richardson-Zaki [12], Gidaspow [3], Syamlal-O'Brien [9], Di Felice [13], and Arastoopour et al. [14] models on a spouted bed where void fraction tendencies lead to more complex behavior of drag forces than normal fluidization systems. While Gidaspow, Syamlal-O-Brien, and Arastoopour et al. models yielded good agreement qualitatively with experimental data, the Gidaspow model was found to best match quantitatively with the experiments. Mahinpey et al [15] also performed a drag model comparison between the Di Felice [13], Gibilaro [16], Koch [17], Syamlal-O'Brien [9], Arastoopour et al. [14], Gidaspow [3], Zhang-Reese [18], and Wen-Yu [10] models. Syamlal-O'Brien and Di Felice adjusted models showed the best agreement quantitatively with experiments. The final drag model comparison of interest, performed by Deza et al [19], compared the Syamlal-O'Brien [9] and Gidaspow [3] drag models for biomass material (ground walnut shell). The study [19] showed that the Gidaspow model can be used to model biomass systems accurately. A summary of momentum exchange coefficients and drag coefficients for each of the drag models mentioned is shown in Table 2.1. Further details about the drag models can be found in the literature.

Table 2.1 Drag model correlations

Drag Model	**K_{sg} =**	**C_D =**
Richardson-Zaki [12]	$\frac{\rho_s \varepsilon_g g}{v_{r,s} \varepsilon_s^{n-1}}$	--
Wen-Yu [10]	$\frac{3}{4} C_D \left(\frac{\varepsilon_s \varepsilon_g \rho_g \lvert \vec{v}_s - \vec{v}_g \rvert}{d_s} \right) \varepsilon_g^{-2.65}$	$\frac{24}{\varepsilon_g Re_s} \left[1 + 0.15 \left(\varepsilon_g Re_s \right)^{0.687} \right]$
Gibilaro et al. [16]	$\left[\frac{17.3}{Re_s} + 0.336 \right] \frac{\rho_g}{d_s} \lvert \vec{v}_s - \vec{v}_g \rvert \varepsilon_s \varepsilon_g^{-1.8}$	--
Syamlal-O'Brien [9]	$\frac{3 \varepsilon_s \varepsilon_g \rho_g}{4 v_{r,s}^2 d_s} C_D \left(\frac{Re_s}{v_{r,s}} \right) \lvert \vec{v}_s - \vec{v}_g \rvert$	$\left(0.63 + \frac{4.8}{\sqrt{\frac{Re_s}{v_{r,s}}}} \right)^2$
Arastoopour et al. [14]	$\left[\frac{17.3}{Re_s} + 0.336 \right] \frac{\rho_g}{d_s} \lvert \vec{v}_s - \vec{v}_g \rvert \varepsilon_s \varepsilon_g^{-2.8}$	--
Di Felice [13]	$\frac{3}{4} C_D \frac{\varepsilon_s \rho_g}{d_s} \lvert \vec{v}_s - \vec{v}_g \rvert \varepsilon_g^{-x}$	$\left(0.63 + \frac{4.8}{\sqrt{Re_s}} \right)^2$
Gidaspow [3]	$\begin{cases} \frac{3}{4} C_D \left(\frac{\varepsilon_s \varepsilon_g \rho_g \lvert \vec{v}_s - \vec{v}_g \rvert}{d_s} \right) \varepsilon_g^{-2.65}, & \varepsilon_g > 0.8 \\ 150 \left(\frac{\varepsilon_s (1 - \varepsilon_g) \mu_g}{\varepsilon_g d_s^2} \right) + 1.75 \left(\frac{\rho_g \varepsilon_s \lvert \vec{v}_s - \vec{v}_g \rvert}{d_s} \right), & \varepsilon_g \leq 0.8 \end{cases}$	$\frac{24}{\varepsilon_g Re_s} \left[1 + 0.15 \left(\varepsilon_g Re_s \right)^{0.687} \right]$
Koch et al. [17]	$\frac{3}{4} C_D \left(\frac{\varepsilon_s \varepsilon_g \rho_g \lvert \vec{v}_s - \vec{v}_g \rvert}{d_s} \right)$	$12 \frac{\varepsilon_g^2}{Re_{s,r}} F$
Zhang-Reese [18]	$\begin{cases} 150 \frac{\varepsilon_s^2 \mu_g}{\varepsilon_g d_s^2} + 1.75 \frac{\varepsilon_s \rho_g}{d_p} \left[\lvert \vec{v}_s - \vec{v}_g \rvert^2 + \frac{8T}{\pi} \right]^{0.5}, & \varepsilon_s < 0.8 \\ \frac{3}{4} C_D \frac{\varepsilon_s \rho_g}{d_p} \left[\lvert \vec{v}_s - \vec{v}_g \rvert^2 + \frac{8T}{\pi} \right]^{0.5} \varepsilon_g^{-2.65}, & \varepsilon_s \geq 0.8 \end{cases}$	$\left(0.28 + \frac{6}{\sqrt{Re_s}} + \frac{21}{Re_s} \right)$

2.4 Particle Characterization

Fluidization behavior of particles can be grouped into four categories: Geldart groups A, B, C, and D [20]. Geldart group A particles have a small mean size (particle diameter) and/or low density (< 1.4 g/cm^3). Group A particles fluidize well, but only after high bed expansion. Group B particles have a mean diameter falling between 40 - 500 μm and particle density between 1.4 - 4.0 g/cm^3. Group B particles are easily fluidized and have small bed expansion before bubbling. Group C constitutes cohesive particulate matter that is extremely difficult to fluidize "normally". These particles tend to lift like a plug since the interparticle forces are stronger than the forces exerted on the particles by the passing gas. Group D particles have very large diameters and/or are very dense and tend to display very poor bed mixing. For the purpose of this research only Geldart group B materials will be studied.

2.5 Fluidization Regimes

Fluidization can be divided into four regime classifications depending on the inlet gas velocity: bubbling, slugging, turbulent, and fast fluidization [6, 21-22]. Bubbling, slugging, and turbulent regimes are shown in Figure 2.3(a-c). As previously mentioned, Geldart group B particle beds expand only slightly as inlet gas velocity increases above the minimum fluidization velocity before bubbling. For a bubbling bed (moderate inlet gas velocity), bubbles much smaller than the bed diameter form and coalesce at the upper surface of the bed. Bubble diameters increase with ascent through the bed [23]. After further increase in the inlet gas velocity, a transition to a slugging bed can be observed where the bubbles in the bed may take up almost the entire bed diameter. Because of this trend, bubbles follow in a single file instead of bubbling as before and the bed expands more than before. The turbulent regime occurs for high inlet gas velocities. In a turbulent bed, the bubbles no longer assume a regular shape, rather they

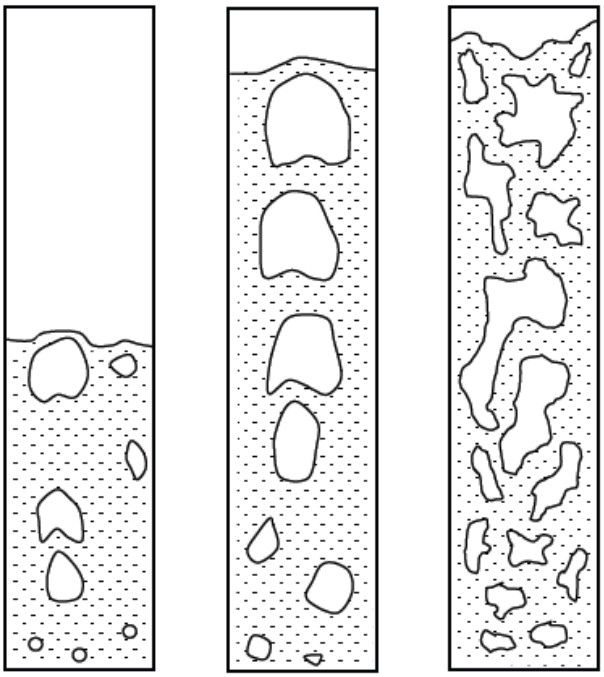

(a) Bubbling (b) Slugging (c) Turbulent

Figure 2.4 Fluidization regimes for fluidized beds [Image reprinted with permission (Deza 2012)]

appear to move chaotically. Also, the bed surface is no longer clearly defined. Increasing the inlet gas velocity passed the turbulent regime produces the fast fluidization regime (not shown), in which the bed has almost no normal characterization. In fast fluidization, bed material may be lost through elutriation or become entrained between inlet jets in the distributor plate.

2.6 Modeling Platforms

There are many vital applications of fluidization, so the need to model fluidized bed dynamics is self-explanatory. Knowing which code is the best for modeling these dynamics is not so straight forward. This section will discuss several publications which are most relevant to the present work.

Benyahia et al. [24] successfully used FLUENT to model gas-solids flow behavior in a circulating fluidized bed using a two-dimensional transient multi-fluid (Eulerian-Eulerian) model incorporating kinetic theory for the solids particles. Fluid catalytic cracking (FCC) particles having a diameter of 76 μm and a density of 1.712 g/cm^3 and air were modeled in a 20 cm diameter reactor having a height of 14.2 m at an inlet gas velocity near minimum fluidization conditions. In this case, the simulations predicted the multiphase flow behavior seen in experiments reasonably well. Only the bed dynamics corresponding to an inlet gas velocity at minimum fluidization or above were explored.

Another study by Taghipour et al. [8] used FLUENT to model a two-dimensional gas-solids fluidized bed comprised of glass beads (Geldart B particles) and air using a multi-fluid model and kinetic theory for solids particles. In this study, different drag models were simulated as well as different values representative of collisional elasticity. The predictions given by simulations compared well with bed expansion properties observed in experiments and compared well qualitatively with flow patterns and instantaneous gas-solids distributions. Pressure drop values corresponding to inlet gas velocities at and above minimum fluidization velocity also compared reasonably well. Pressure drop values corresponding to inlet gas velocities below minimum fluidization velocity were very far off from those values measured during the experiments. This phenomenon is one of the facets to be explored herein, and is again mentioned in a study performed by Sahoo et al. [25]. The study [25] examined the effects of varying bed material and static bed height. The particles that were studied had very large diameters (Geldart D). It was again observed that the time-averaged pressure drop data for the simulations matched the experiments well for velocities exceeding minimum fluidization, but was not the case for velocities lower than minimum fluidization.

Herzog et al. [26] conducted a study which compared the results of modeling fluidized bed hydrodynamics with the open source software packages OpenFOAM and MFIX against the results obtained using FLUENT. The basis of experimental comparison for this study was taken from the numerical validation study previously mentioned by Taghipour et al. [8]. Herzog et al. [26] concluded that MFIX and FLUENT gave good comparisons with experimental data in the bubbling regime and also showed good agreement with each other for pressure drop. The curves of pressure drop versus inflow velocity reported by Herzog et al. correctly showed an increasing pressure drop trend until the point of minimum fluidization and compared reasonably well with the experimental data in the unfluidized regime. It is important to note that the model parameters which need to be specified in FLUENT were not revealed in the publication.

Chapter 3 Methodology

The multiphase flow theory of the commercial code ANSYS FLUENT v12.0 is discussed in this chapter [27-28]. The theory will be broken into sections consisting of governing equations, numerical approach, and initial and boundary conditions.

3.1 Governing Equations

An Eulerian-Eulerian multiphase flow model is chosen to simulate granular flow in a fluidized bed reactor. The Eulerian-Eulerian model represents each phase as interpenetrating continua, where each phase is separate, yet interacting, and the volume of a phase cannot be occupied by another phase. The assumption of interpenetrating continua introduces the concept of phasic volume fractions, whereby the sum of the fraction of space occupied by each of the phases equals one. The phasic volume fraction equation is given by:

$$\sum_{q=1}^{n} \varepsilon_q = 1 \qquad 3.1$$

where n represents the total number of phases and ε_q represents the volume fraction of each phase, q. The two phases correspond to the gas phase, g, or primary phase, and the solids phase, s, or secondary phase. The volume fraction of the gas is most commonly referred to as the void fraction, ε_g. The effective density of each phase q is given by:

$$\hat{\rho}_q = \varepsilon_q \rho_q \qquad 3.2$$

where ρ_q is the material density of each phase. The Eulerian-Eulerian model allows for incorporation of multiple secondary solids phases.

The laws of conservation of mass and momentum are satisfied, respectively, by each phase. Thus, the Eulerian-Eulerian model solves a set of n momentum and continuity equations, causing it to be one of the most complex of the multiphase models available.

3.1.1 Conservation of Mass

The continuity equation for a phase q is:

$$\frac{\partial}{\partial t}\left(\varepsilon_q \rho_q\right) + \nabla \cdot \left(\varepsilon_q \rho_q \vec{v}_q\right) = \sum_{p=1}^{n}\left(\dot{m}_{pq} - \dot{m}_{qp}\right) + S_q \qquad 3.3$$

where n represents the number of phases, $\vec{v}_q$ is the velocity of phase q, $\dot{m}$ represents mass transfer between phases, and S_q represents a mass source term for each phase, which is zero by default. Assuming a closed system with no mass transfer between phases, all of the right hand side terms vanish reducing continuity to:

$$\frac{\partial}{\partial t}\left(\varepsilon_q \rho_q\right) + \nabla \cdot \left(\varepsilon_q \rho_q \vec{v}_q\right) = 0 \qquad 3.4$$

3.1.2 Conservation of Momentum

The momentum equation for gas phase g is written as:

$$\frac{\partial}{\partial t}\left(\varepsilon_g \rho_g \vec{v}_g\right) + \nabla \cdot \left(\varepsilon_g \rho_g \vec{v}_g \vec{v}_g\right) =$$

$$-\varepsilon_g \nabla p + \nabla \cdot \bar{\bar{\tau}}_g + \varepsilon_g \rho_g \vec{g} + \sum_{s=1}^{m}\left(\vec{R}_{sg} + \dot{m}_{sg}\vec{v}_{sg} - \dot{m}_{gs}\vec{v}_{gs}\right) + \left(\vec{F}_g + \vec{F}_{lift,g} + \vec{F}_{vm,g}\right) \qquad 3.5$$

where m represents the number of solids phases. The first term on the left hand side of the momentum equation represents the unsteady acceleration and the second term represents the convective acceleration of the flow. The first term on the right hand side of Equation 3.5

accounts for pressure changes, where p is the pressure shared by all phases. The second term is a stress-strain tensor term, represented by:

$$\bar{\bar{\tau}}_g = \varepsilon_g \mu_g \left(\nabla \vec{v}_g + \nabla \vec{v}_g^T\right) + \varepsilon_g \left(\lambda_g - \frac{2}{3}\mu_g\right) \nabla \cdot \vec{v}_g \bar{\bar{I}} \qquad 3.6$$

where μ_g and λ_g are the shear and bulk viscosity of gas phase g, $\nabla \vec{v}_g^T$ is the transpose of the velocity gradient, and $\bar{\bar{I}}$ is the identity matrix. The third term on the right hand side of Equation 3.5 represents gravitational force. The fourth group of terms inside the summation includes an interaction force between gas and solids phases, $\vec{R}_{sg}$, as well as terms representing mass transfer between phases. The fifth and final grouping of terms includes an external body force, $\vec{F}_g$, a lift force, $\vec{F}_{lift,g}$, and a virtual mass force, $\vec{F}_{vm,g}$. For the purposes of the present research, the mass transfer terms, external body force, lift force, and virtual mass force terms are all zero, simplifying the momentum equation for the gas phase to the following form:

$$\frac{\partial}{\partial t}\left(\varepsilon_g \rho_g \vec{v}_g\right) + \nabla \cdot \left(\varepsilon_g \rho_g \vec{v}_g \vec{v}_g\right) = -\varepsilon_g \nabla p + \nabla \cdot \bar{\bar{\tau}}_g + \varepsilon_g \rho_g \vec{g} + \sum_{s=1}^{m} \vec{R}_{sg} \qquad 3.7$$

where the interaction force, $\vec{R}_{pq}$, is represented by:

$$\sum_{s=1}^{m} \vec{R}_{sg} = \sum_{s=1}^{m} K_{sg}\left(\vec{v}_s - \vec{v}_g\right) \qquad 3.8$$

as the product of the interphase momentum exchange coefficient, K_{sg}, and the slip velocity. The momentum equation for the s^{th} solids phase is written as:

$$\frac{\partial}{\partial t}\left(\varepsilon_s \rho_s \vec{v}_s\right) + \nabla \cdot \left(\varepsilon_s \rho_s \vec{v}_s \vec{v}_s\right) =$$

$$-\varepsilon_s \nabla p - \nabla p_s + \nabla \cdot \bar{\bar{\tau}}_s + \varepsilon_s \rho_s \vec{g} + \sum_{p=1}^{n} \left(\vec{R}_{ps} + \dot{m}_{ps} \vec{v}_{ps} - \dot{m}_{sp} \vec{v}_{sp}\right) + \left(\vec{F}_s + \vec{F}_{lift,s} + \vec{F}_{vm,s}\right) \qquad 3.9$$

where p_s is the solids pressure, and $\vec{R}_{ps}$ is the interaction force between the gas phase or solids phase p and solids phase s. All other terms are defined similarly to those in Equation 3.5, and neglecting mass transfer, the solids phase momentum equation simplifies to the following form:

$$\frac{\partial}{\partial t}(\varepsilon_s \rho_s \vec{v}_s) + \nabla \cdot (\varepsilon_s \rho_s \vec{v}_s \vec{v}_s) = -\varepsilon_s \nabla p - \nabla p_s + \nabla \cdot \bar{\bar{\tau}}_s + \varepsilon_s \rho_s \vec{g} + \sum_{p=1}^{n} \vec{R}_{ps} \qquad 3.10$$

where the interaction force, $\vec{R}_{ps}$, is represented by:

$$\sum_{p=1}^{n} \vec{R}_{ps} = \sum_{p=1}^{n} K_{ps}(\vec{v}_p - \vec{v}_s) \qquad 3.11$$

as the product of the momentum exchange coefficient, K_{ps}, and the slip velocity, and where $K_{ps} = K_{sp}$. For the approaches examined herein, only a singular solids phase is used. In light of this, Equations 3.8 and 3.11 are equivalent expressions.

3.1.2.1 Gas-Solid Interaction

The gas-solids momentum exchange coefficient, K_{sg}, can be written as:

$$K_{sg} = \frac{\varepsilon_s \rho_s f}{\tau_s} \qquad 3.12$$

where the definition of f depends on the exchange-coefficient model chosen, and τ_s, the particulate relaxation time, is defined as:

$$\tau_s = \frac{\rho_s d_s^2}{18 \mu_g} \qquad 3.13$$

where d_s is the diameter of the particles of solids phase s. The definition of f includes a drag coefficient, C_D, based on a relative Reynolds number, Re_s. The Gidaspow drag model [3] is chosen to calculate the gas-solids momentum exchange coefficient, and is a combination of the

Wen and Yu model [10] and the Ergun equation [7]. The Gidaspow model is characterized by the following:

$$K_{sg} = \begin{cases} \frac{3}{4} C_D \left(\frac{\varepsilon_s \varepsilon_g \rho_g \left| \vec{v}_s - \vec{v}_g \right|}{d_s} \right) \varepsilon_g^{-2.65}, & \varepsilon_g > 0.8 \\ 150 \left(\frac{\varepsilon_s (1 - \varepsilon_g) \mu_g}{\varepsilon_g d_s^2} \right) + 1.75 \left(\frac{\rho_g \varepsilon_s \left| \vec{v}_s - \vec{v}_g \right|}{d_s} \right), & \varepsilon_g \leq 0.8 \end{cases} \quad 3.14$$

where the coefficient of drag [29] is further defined for a smooth particle as:

$$C_D = \begin{cases} \frac{24}{\varepsilon_g Re_s} \left[1 + 0.15 (\varepsilon_g Re_s)^{0.687} \right], & \mathrm{Re_s} < 1000 \\ 0.44, & \mathrm{Re_s} \geq 1000 \end{cases} \quad 3.15$$

where Re_s is a function of the slip velocity of the solids phase as follows:

$$Re_s = \frac{\rho_g d_s \left| \vec{v}_s - \vec{v}_g \right|}{\mu_g} \quad 3.16$$

The Gidaspow model is well-suited for densely packed fluidized bed applications.

3.1.2.2 Solids Pressure

For granular flow in a compressible regime, or when the solids volume fraction is below its maximum value, a solids pressure is calculated for the second pressure gradient term of Equation 3.10. The Lun et al. [30] solids pressure equation contains two terms: a kinetic term and a particle collision term, and is of the following form:

$$p_s = \varepsilon_s \rho_s \Theta_s + 2\rho_s (1 + e_{ss}) \varepsilon_s^2 g_{0,ss} \Theta_s \quad 3.17$$

where Θ_s is granular temperature, e_{ss} is the coefficient of restitution for particle collisions, and $g_{0,ss}$ is the radial distribution function. The granular temperature is not a physical temperature, in the classical sense, but rather is proportional to the kinetic energy of random particle motion.

The radial distribution function governs the transition from the compressible regime to the incompressible regime, where the solids volume fraction equals the maximum allowable solids volume fraction.

3.1.2.3 Solids Shear Stresses

The solids stress tensor, $\bar{\bar{\tau}}_s$, is defined as that of the gas phase stress tensor of Equation 3.6. The stress tensor contains shear and bulk viscosities generated by particle momentum exchange during collision and translation. A frictional viscosity is included to account for a transition between viscous and plastic regimes that occurs when the solids volume fraction approaches its maximum value. The shear viscosity, or granular viscosity, is then defined as:

$$\mu_s = \mu_{s,col} + \mu_{s,kin} + \mu_{s,fr} \tag{3.18}$$

where the three viscosity components are collisional, kinetic, and frictional, respectively.

The solids bulk viscosity, or granular bulk viscosity, accounts for resistance to compression and expansion of the solids phase particles, and is of the form:

$$\lambda_s = \frac{4}{3}\varepsilon_s \rho_s d_s g_{0,ss}(1 + e_{ss})\left(\frac{\Theta_s}{\pi}\right)^{\frac{1}{2}} \tag{3.19}$$

3.1.3 Granular Temperature

As previously mentioned, the granular temperature, Θ_s, of a solids phase s is proportional to the kinetic energy of the collisions and translations of the particles. The transport equation is derived from kinetic theory and is of the following form:

$$\frac{3}{2}\left[\frac{\partial}{\partial t}(\varepsilon_s \rho_s \Theta_s) + \nabla \cdot (\varepsilon_s \rho_s \vec{v}_s \Theta_s)\right] = \left(-p_s \bar{\bar{I}} + \bar{\bar{\tau}}_s\right) : \nabla \vec{v}_s + \nabla \cdot \left(k_{\Theta_s} \nabla \Theta_s\right) - \gamma \Theta_s + \varphi_{ps} \tag{3.20}$$

where $\left(-p_s \bar{\bar{I}} + \bar{\bar{\tau}}_s\right) : \nabla \vec{v}_s$ is the generation of energy by the solids stress tensor, $k_{\Theta_s} \nabla \Theta_s$ is the diffusion of energy and k_{Θ_s} is the diffusion coefficient, $\gamma \Theta_s$ is the collisional dissipation of

energy, and φ_{ps} is the energy exchange between the fluid or solids phase p and the solids phase s. An algebraic formulation is used to solve the granular energy equation, whereby convection and diffusion in the transport equation are neglected.

3.2 Numerical Approach

FLUENT solves governing integral equations for conservation of mass and momentum. The methodology employs a finite volume approach for flow solutions, which is beneficial for local satisfaction of the conservation equations and for relatively coarse grid modeling.

3.2.1 Pressure-Based Solver Algorithm

A pressure-based solver is employed to solve phasic momentum equations, shared pressure, and phasic volume fraction equations in a segregated manner. The phase-coupled semi-implicit method for pressure linked equations (PC-SIMPLE) algorithm is utilized, which is an extension of the SIMPLE algorithm [31] developed for multiphase flows. In the PC-SIMPLE method, velocities are solved coupled by phases, yet in a segregated manner. A block algebraic multigrid scheme is then used to solve a vector equation of the velocity components of all phases

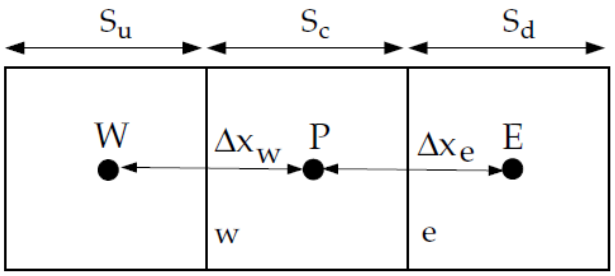

Figure 3.1 One-dimensional control volume used in QUICK scheme

simultaneously. A pressure correction equation is then built based on total volume continuity

rather than conservation of mass. Pressure and velocity corrections are then applied to satisfy the total volume continuity constraint.

3.2.2 Spatial Discretization

Discrete values of a scalar quantity ϕ are stored at cell centers. Face values, ϕ_f, however, are required for convection terms and must be interpolated from cell center values. Face values are generated using upwind schemes, by which the face value ϕ_f is derived from quantities in the adjacent upstream cell. For spatial discretization, a second-order upwind scheme is chosen for the momentum equations, and quadratic upwind interpolation for convective kinematics (QUICK) scheme [32] is chosen for volume fraction.

The second-order upwind approach computes desired quantities at cell faces using a multidimensional linear reconstruction approach. In this approach, Taylor series expansions of a cell-centered solution about the cell centroid give higher-order accuracy at cell faces. In a second-order upwind scheme, a face value, ϕ_f, is computed using the following:

$$\phi_f = \phi + \nabla\phi \cdot \vec{r} \tag{3.21}$$

where ϕ and $\nabla\phi$ are the cell-centered value and its gradient in the upstream cell, and $\vec{r}$ is the displacement vector from the upstream cell centroid to the face centroid.

The QUICK scheme is useful for quadrilateral meshes where unique upstream and downstream faces and cells are easily identified, as shown in Figure 3.1. The QUICK scheme is based on a weighted average of second-order upwind and central interpolations of the variable. For flow from left to right, a face value for face e can be written as:

$$\phi_e = \theta\left[\frac{S_d}{S_c + S_d}\phi_P + \frac{S_c}{S_c + S_d}\phi_E\right] + (1-\theta)\left[\frac{S_u + 2S_c}{S_u + S_c}\phi_P - \frac{S_c}{S_u + S_c}\phi_W\right] \tag{3.22}$$

where each cell has a size S, points W, P, and E represent cell centers, and subscripts u, c, and d represent upwind, center, and downwind cells. If a θ value of unity is substituted into Equation 3.22, a central second-order interpolation results, whereas a θ value of zero results in a second-order upwind interpolation. In the research at hand, a variable solution-dependent value of θ is utilized in order to avoid introducing artificial extrema.

3.2.3 Initial and Boundary Conditions

3.2.3.1 Initial Conditions

Initial conditions may not affect the steady-state solution that is desired in fluidized bed modeling, however, strategically chosen initial conditions help to ensure convergence of the solution. There are two types of initial conditions which must be specified: solids volume fraction in the packed bed and freeboard, and y-velocity (vertical velocity) of the gas phase in the packed bed and freeboard. The solids volume fraction in the packed bed is based on experimental measurement or solely on solids phase material properties, and the solids volume fraction in the freeboard is initially set to zero assuming only gas. The y-velocity of the gas phase in the packed bed is calculated through a steady state volumetric flow rate balance in which the flow rate entering the fluidized bed reactor is equated to the flow rate through the packed bed portion (having both solids and gas phases) of the reactor as follows:

$$\forall_{inlet} U_{inlet} = \forall_{pbg} U_{pbg} \tag{3.23}$$

where $\forall$ is volume, U is velocity, and the subscript pbg corresponds to packed bed gas phase. Note that U_{pbg} in this case represents the superficial velocity of the gas (see Equation 2.1). Rearranging Equation 3.23 gives the following:

$$U_{pbg} = U_{inlet}\left(\frac{\forall_{inlet}}{\forall_{pbg}}\right) \tag{3.24}$$

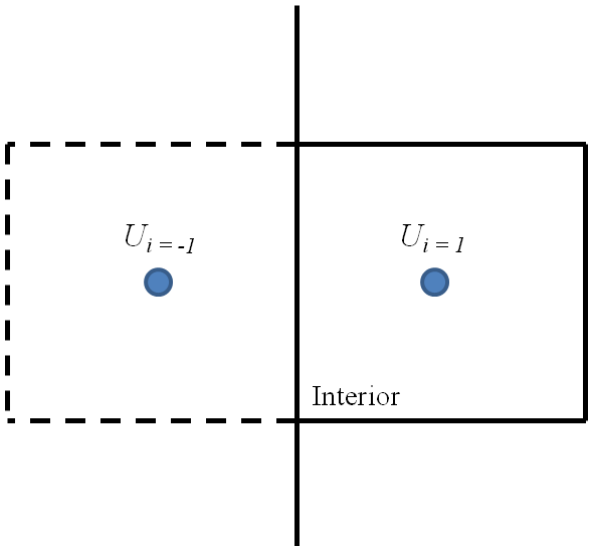

Figure 3.2 Example of no slip wall boundary condition

where the ratio of the packed bed volume to the inlet volume is equivalent to the void fraction, or gas phase volume fraction, simplifying Equation 3.24 to the following form:

$$U_{pbg} = \frac{U_{inlet}}{\varepsilon_g} \tag{3.25}$$

The y-velocity of the gas phase in the freeboard is specified as being equal to the inlet gas velocity.

3.2.3.2 Boundary Conditions

The gas inlet of a fluidized bed is generally characterized by a distributor plate having evenly distributed holes such as to enforce a nearly uniform flow. Therefore, the inlet boundary condition is modeled as a velocity-inlet having a uniform vertical velocity profile, as well as having constant pressure. The volume fraction of solids at the inlet is zero. The outlet boundary condition is specified as having ambient pressure, and a backflow solids volume fraction equal to zero. The wall boundary condition for the gas phase inside the fluidized bed reactor is no-slip,

which means that the relative velocity of the air along the wall is zero. The no-slip condition is demonstrated for a cell bordering a wall by:

$$U_{i=-1} = -U_{i=1} \tag{3.26}$$

where the index i represents the x-direction, $i = 1$ is a cell in the reactor domain bordering the wall, and $i = -1$ is a ghost cell opposing the interior cell and adjacent to the wall cell, as shown in Figure 3.2. The solids phase boundary condition for the reactor walls is specified as free slip.

Chapter 4 Grid Resolution Study

It is of key importance when performing CFD to check the accuracy of solutions through a grid resolution study. A grid resolution study is a balancing act between the coarseness of the grid and the computation time required for solution. Following an obvious line of reasoning, the coarser the grid, the less computation time required, and vice versa. The key parameter involved is what percentage of relative error is tolerable. The following chapter will outline the results of a grid resolution study using a glass bead fluidized bed.

4.1 Experimental Setup and Procedure

The bubble dynamics inside of a fluidized bed are very important to capture. It is experimentally unsound to use invasive monitoring techniques due to obstruction of regular bed dynamics. Therefore, it is necessary to utilize a noninvasive method. In recent years, images revealing the gas-solids distributions of fluidized beds have been ascertained through X-ray computed tomography (CT) and X-ray fluoroscopy (radiography) [19, 33-35]. Franka et al. [33] captured gas-solids distribution images using these technologies with several different bed materials including glass beads, melamine, walnut shell, and corncob. The images revealed that glass beads fluidized the most uniformly, constituting the choice of material for the present grid resolution study.

A schematic of the experimental fluidized bed apparatus is shown in Figure 1 of Franka et al. [33] with details of the setup used in the experiments and serves as the basis of comparison for the grid resolution study simulations. The bed chamber is an acrylic tube with an internal diameter of 9.5 cm, a bed height of 40 cm, and a static granular bed height of 10 cm. Air enters an air plenum chamber through an air inlet tube and is distributed into the plenum chamber by an inlet air distributor . The air then passes through a distributor plate and screen . The distributor

plate has 100, 10 mm diameter holes, equally spaced. On top of the distributor plate lies a 45 mesh screen which prevents bed media from clogging the distributor plate holes. Pressure taps are strategically placed vertically along the apparatus for monitoring pressure difference across certain lengths of the bed.

Glass beads were chosen as the bed material for this study because the fluidization is well defined. Glass beads are a near ideal particle to model due to high sphericity, elasticity of collisions, and uniform density. The minimum fluidization velocity, U_{mf}, for the glass bead bed was measured experimentally. The bed was first supplied with an inlet gas velocity of 28 cm/s and the inflow was subsequently decreased by increments of 1.2 cm/s. The pressure drop between the plenum chamber and the outlet of the bed chamber was measured for each velocity. Beginning with a faster airflow and then slowing down eliminates any resistance from a packed bed to fluidize, which can cause problems in identifying the actual minimum fluidization velocity. Since the pressure drop was recorded from a point below the distributor plate, a dry run, or empty bed experiment was performed in order to subtract any pressure drop generated by the distributor plate. Just as seen in Figure 2.3, the pressure drop data seen in the experiments remains constant until a certain inlet gas velocity when it begins to linearly decrease. The point at which this transition occurs is marked as the minimum fluidization velocity, or 19.9 cm/s for the glass bead fluidized bed.

4.2 Computational Setup and Bed Parameters

A simple schematic of the experimental apparatus design used for the simulations is shown in Figure 4.1. The apparatus is modeled as a two-dimensional geometry, which represents the center-plane of the cylindrical experimental reactor. The dimensions of the bed chamber remain the same: 9.5 cm internal diameter, 40 cm total bed height, and a 10 cm static

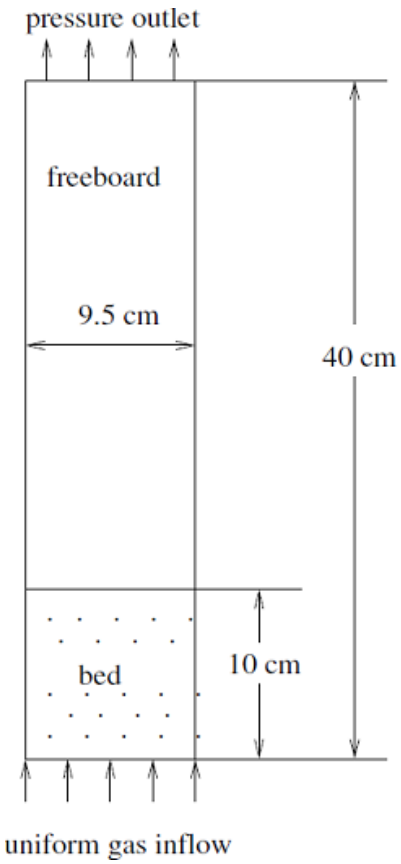

Figure 4.1 Schematic of the primary portion of the fluidized bed for the grid resolution study [Image reprinted with permission (Deza 2012)]

Table 4.1 Glass bead bed properties

Property	**Value**
d_p (cm)	0.055
ρ_p (g/cm^3)	2.60
ρ_b (g/cm^3)	1.63
ψ (-)	0.9
$\boldsymbol{e}$ (-)	0.95
U_{mf} (cm/s)	19.9
ε_g^* (-)	0.373
U_g (cm/s)	25.8

granular bed height. Particle and flow properties are summarized in Table 4.1. The inlet gas

Table 4.2 Grid resolution parameters

No. cells	Δx (cm)	Δy (cm)
19×80	0.50	0.50
38×80	0.25	0.50
38×160	0.25	0.25
76×320	0.125	0.125

velocity, or superficial gas velocity, is set as 25.8 cm/s, or 1.3 U_{mf} and an initial void fraction of 0.373 is specified. The outlet is modeled as atmospheric. A no-slip condition is specified for gas-wall interactions, and a free-slip condition is specified for particle-wall interactions.

4.3 Grid Resolutions and Case Results

For this study, four grid resolution cases were chosen with meshes having rectangular cells of aspect ratios of either 1:1 or 1:2. The dimensions of the cells for each of the four cases can be seen in Table 4.2. Simulations for this study were run using a time step of 10^{-4} seconds from 0 to 40 seconds, with time-averaging taken between 5 and 40 seconds over 3500 time realizations (every 0.01 seconds). Figure 4.2 shows instantaneous void fraction contours for each grid resolution at a flow time of 20 seconds. The contours shown in Figure 4.1 really highlight visually the necessity of performing a grid resolution study. It is clear from these contours that increasing the number of cells increases the clarity and definition of the bubbles seen in the bed. The bubbles present in the 19×80 and 38×80 contours do not show true voids where only gas is present. The interior of the bubbles in the 19×80 case appear light green, insinuating that some bed material is still present. On the other hand, the 76×320 case shows bubbles having light yellow and red interiors, meaning that very little or no sand is present. The 38×160 and 76×320 contours are comparable in definition. Void fraction profiles for bed

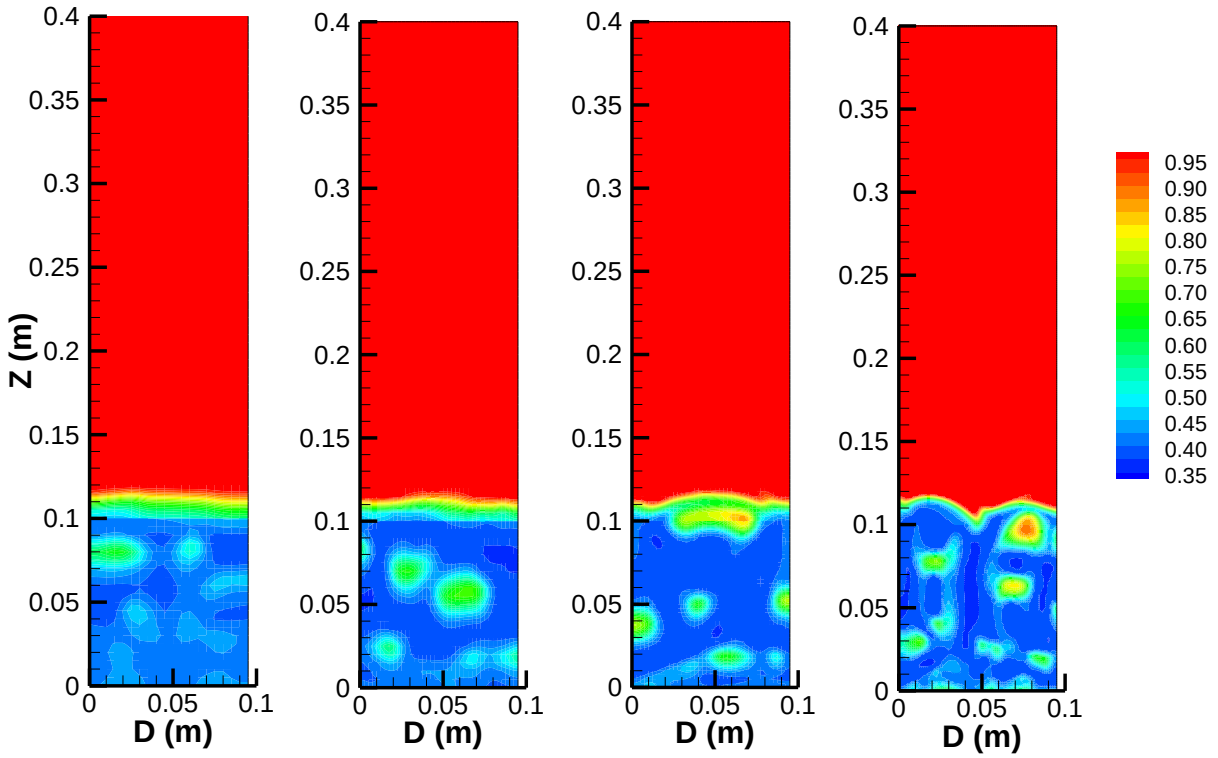

(a) 19×80 (b) 38×80 (c) 38×160 (d) 76×320

Figure 4.2 Instantaneous void fraction contours for a flow time of 20 seconds for each of the grid resolutions (a)-(d)

heights of 4 cm and 8 cm are shown in Figure 4.3 for each grid resolution. Generally, all of the meshes yield results that compare reasonably well. The coarsest grid, 19×80 is the greatest outlier, the discrepancy of which can be seen more so in Figure 4.2(b). It is interesting to note that the change in aspect ratio from the 38×160 mesh to the 38×80 mesh makes almost no difference. For the purposes of this study, however, the equal aspect ratio meshes will be examined.

A Richardson's Extrapolation was performed between each of the grid sizes. The coarsest grid yields the largest relative error which is less than 3%. The relative error between

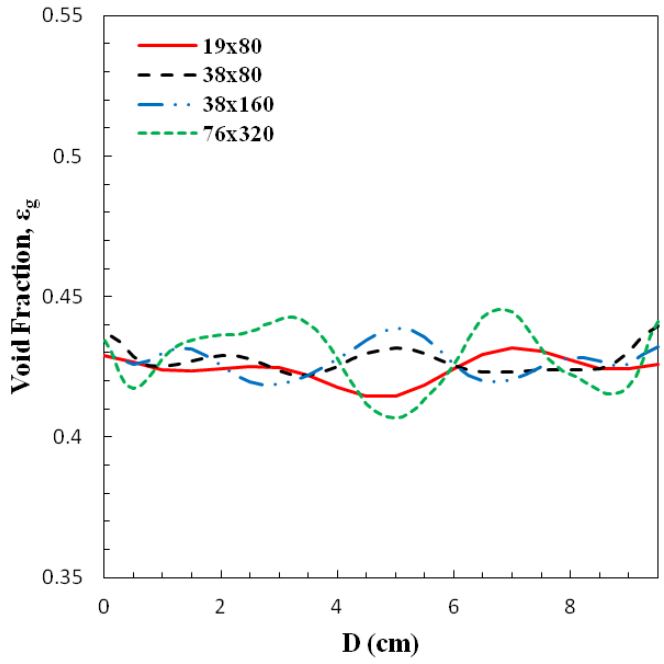

(a) z = 4 cm

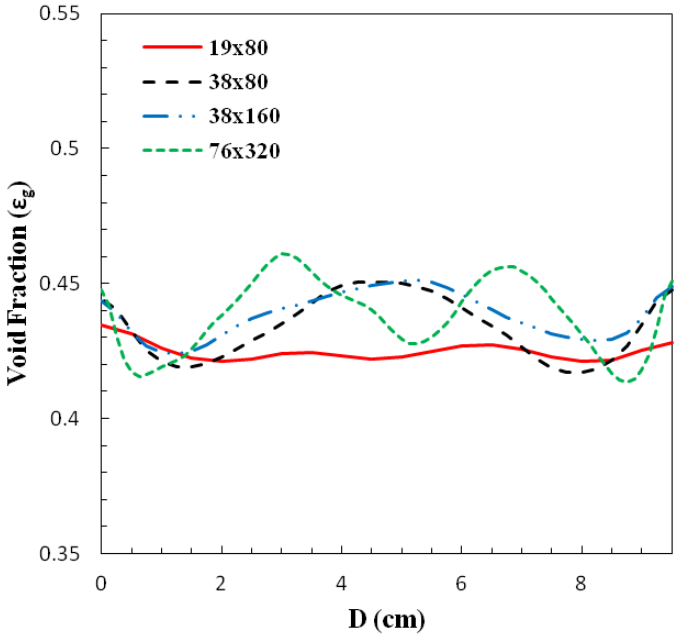

(a) z = 8 cm

Figure 4.3 Time-averaged void fraction profiles of simulation data for each different grid resolution at (a) z = 4 cm and (b) z=8 cm

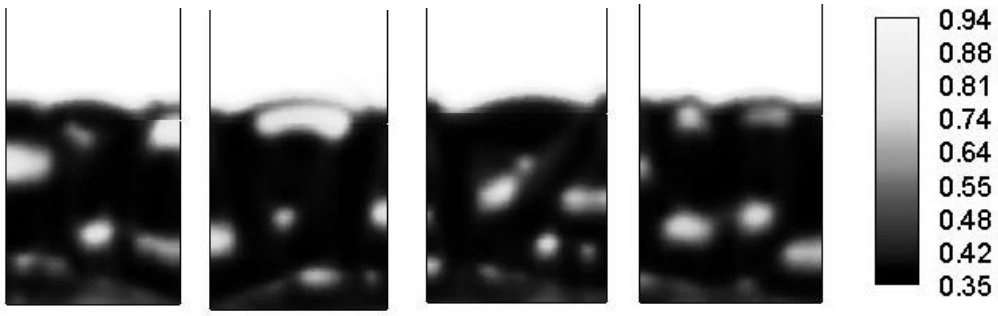

(a) 10 s (b) 20 s (c) 30 s (d) 40 s

Figure 4.4 Instantaneous void fraction contours for the glass bead fluidized bed. Images are displayed in a time progression from (a) 10 s, (b) 20 s, (c) 30 s, and (d) 40 s

the next two finer meshes, 38×160 and 76×320, is significantly lower, falling below 0.2%. In light of this calculation, all data presented in this chapter will correspond to the 38×160 mesh.

Instantaneous void fraction contours at 10 second increments are shown in Figure 4.4. The images in Figure 4.4 can be compared with the images in Figure 3 of Deza et al. [19]. Deza et al. also performed a grid resolution study with the code MFIX using the experimental results of Franka et al. [19] as a basis for comparison. Deza et al. presents images from radiographs taken from the experiments and corresponding simulations. The X-ray images qualitatively show bubble locations and size, but do not represent void fraction in any quantitative manner. It is evident from Figure 4.4 that the simulations and experiments [19] are in very good qualitative agreement in terms of bubble size and general location. It is also visible that the typical bubbling bed behavior is occurring where small bubbles form near the bottom of the bed and coalesce near the top of the bed. The contours of Figure 4.4 also match well with the contours representative of the MFIX simulations.

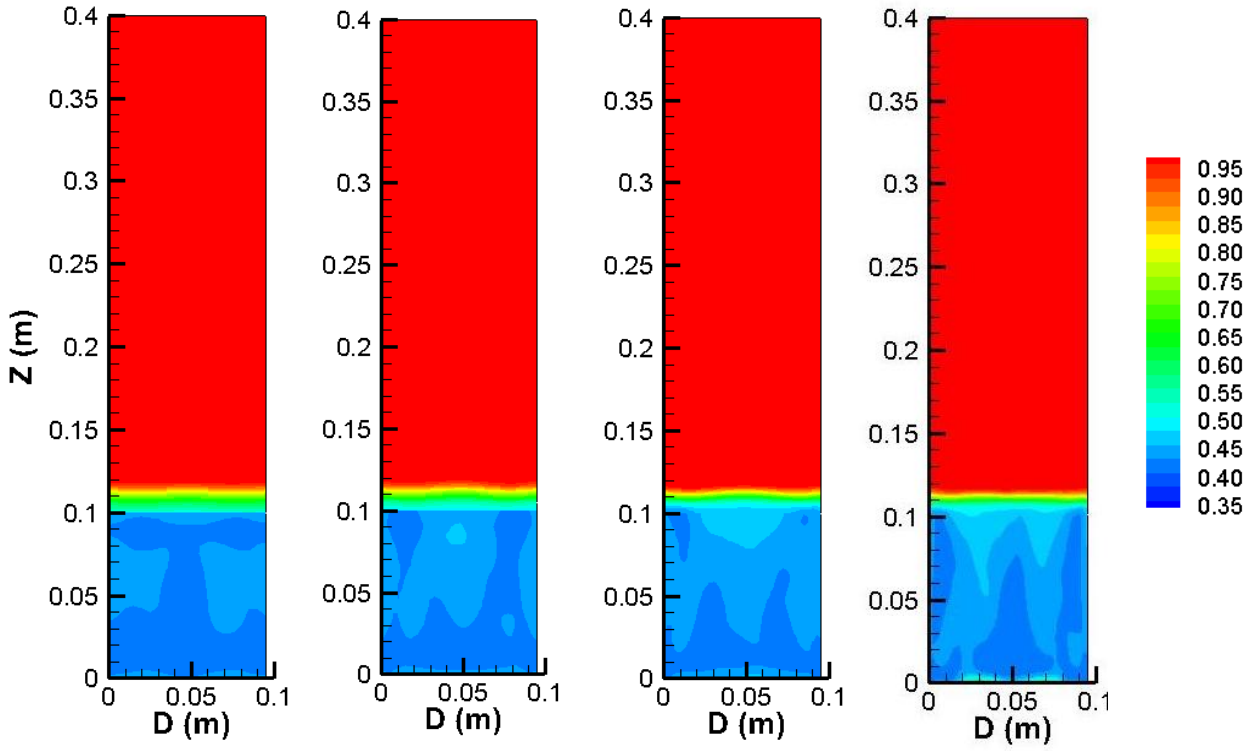

(a) 19×80 (b) 38×80 (c) 38×160 (d) 76×320

Figure 4.5 Time-averaged void fraction contours of the glass bead bed of the simulated cases (a)-(d)

Figure 4.5 shows time-averaged void fraction contours for each grid resolution. The coarsest mesh, 19×80, shows unrealistic bed behavior where bed material agglomerates near the bottom and top of the bed and the only less dense portions are seen in the middle of each side of the bed. The 38×80 case shows some of the same characteristics as the coarsest mesh, but also shows a region less dense in the upper middle of the bed. The 38×160 and 76×320 cases show a more homogeneous flow pattern in which bubbles are more evenly distributed. Only the 76×320 mesh really highlights bubble formation at the base of the bed (also see Figure 4.2(d)). The contours of Figure 4.5 can be compared with Figure 4 of Deza et al. [19], where subfigures (a)-(c) represent contours of MFIX simulations and subfigures (d)-(e) represent X- and Y-slice CT

images taken from the experiments. The finest mesh compares the best with the CT image slices, but the 38×160 mesh also compares reasonably well.

Void fraction profiles for bed heights of 4 cm and 8 cm, as in Figure 4.3, are shown again in Figure 4.6, only now in combination with the experimental data [19]. The main conclusion to draw from the plots in Figure 4.6 is that the local time-averaged void fractions of the simulations agree in general order of magnitude with those of the experimental slices. Also, the simulated data seems to draw a middle or average line through the experimental profiles. If the experimental data were averaged across the bed diameter to a single value, the discrepancy between the simulations and experiments would appear much smaller. One occurrence to notice is how the profiles of the experimental data are more erratic at a bed height of 4 cm as compared with a bed height of 8 cm. Such a trend has been observed before, and is likely due to the fact that the distributor plate can have a significant effect on the bed dynamics near the bottom of the bed [8]. It follows reason that the trend would not be captured in the simulated data because the distributor plate is not modeled in the simulations for simplicity.

As previously noted, if the experimental data were averaged across the bed diameter then the local variations would not be as noticeable. Figure 4.7 represents just that, a time- and plane-averaged plot of void fraction versus bed height for each of the simulated cases as well as each of the experimental slices. It is apparent from Figure 4.7 that the bed expands only slightly higher in the simulations than in the experiments, where the bed expansion was measured to be 11.2 cm. Each of the simulated cases falls generally between the X- and Y-slices from the experiments. Only the coarsest grid, 19×80, protrudes slightly outside the bounds of the experimental data. Each of the three finer meshes appear to lie directly on top of one another.

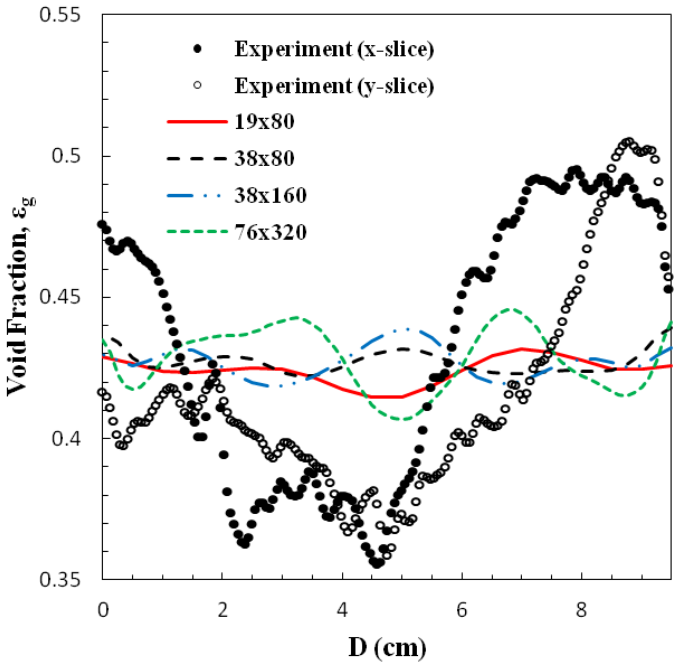

(a) z = 4 cm

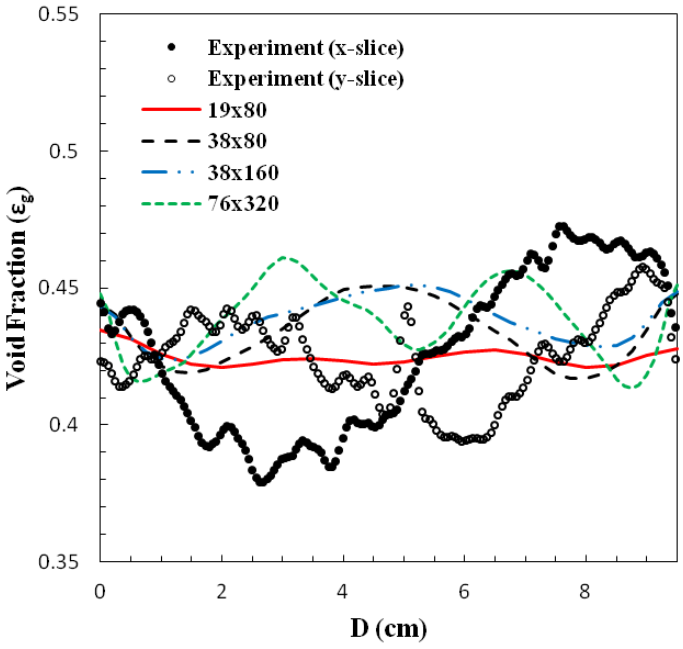

(b) z = 8 cm

Figure 4.6 Time-averaged void fraction profiles comparing glass bead simulations with experimental data at (a) z = 4 cm and (b) z = 8 cm

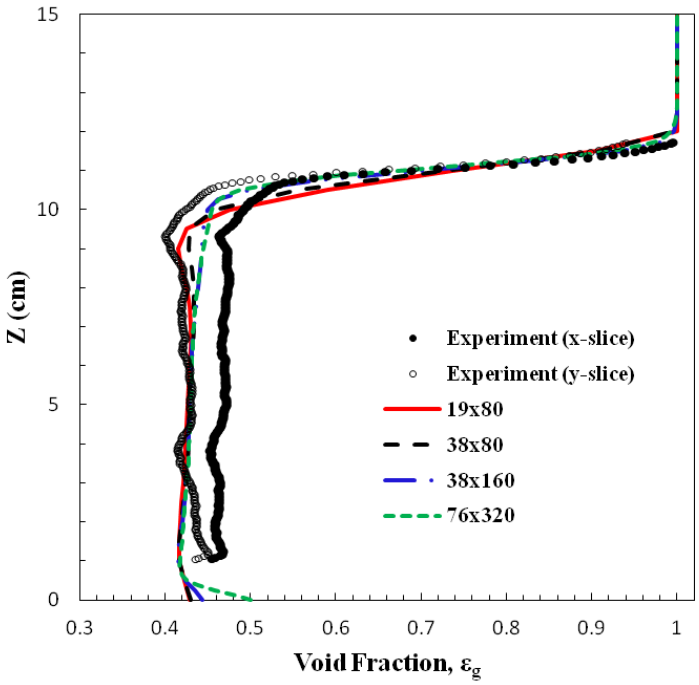

Figure 4.7 Bed height versus time- and plane-averaged void fraction for each grid resolution and experimental data

It is important in choosing the appropriate grid resolution to consider qualitative results, like void fraction contours, and quantitative results, like void fraction profiles and error calculations (Richardson's extrapolation). Reasonable agreement between the simulated data and experimental data in both of these areas allows for an informed decision to be made. From the contents of this study, it is determined that the 38x160 mesh having square cells of side length 0.25 cm is the best to use.

Chapter 5 Modeling Approach Comparison

Computational modeling of fluidized beds encompasses a great deal of simplifications from experimental setups and bed material characteristics, especially when the experiments deal with irregular particles such as biomass particles. The following chapter will compare and contrast various methods for better predicting fluidized bed hydrodynamics of biomass particles.

5.1 Alternative Drag Model

The following chapter includes a parametric study where certain parameters of the simulation case setup are changed. One of the parameters to be changed is the drag model. An alternative to the Gidaspow drag model (see Equation 3.14), the Syamlal-O'Brien drag model [9], is of the following form:

$$f = \frac{C_D Re_s \varepsilon_g}{24 v_{r,s}^2} \tag{5.1}$$

where f is the same as in Equation 3.12 and the coefficient of drag, C_D, has the form:

$$C_D = \left(0.63 + \frac{4.8}{\sqrt{\frac{Re_s}{v_{r,s}}}} \right)^2 \tag{5.2}$$

and where Re_s is a function of the slip velocity of the solids phase as follows:

$$Re_s = \frac{\rho_g d_s |\vec{v}_s - \vec{v}_g|}{\mu_g} \tag{5.3}$$

The fluid-solids exchange coefficient has the form:

$$K_{sg} = \frac{3 \varepsilon_s \varepsilon_g \rho_g}{4 v_{r,s}^2 d_s} C_D \left(\frac{Re_s}{v_{r,s}} \right) |\vec{v}_s - \vec{v}_g| \tag{5.4}$$

where $v_{r,s}$ is the terminal velocity correlation for the solids phase as follows:

$$v_{r,s} = 0.5(A - 0.06Re_s + \sqrt{(0.06Re_s)^2 + 0.12Re_s(2B - A) + A^2} \quad 5.5$$

and where

$$A = \varepsilon_g^{4.14} \quad 5.6$$

and

$$B = 0.8\varepsilon_g^{1.28} \quad 5.7$$

for $\varepsilon_g \leq 0.85$, and

$$B = \varepsilon_g^{2.65} \quad 5.8$$

for $\varepsilon_g \geq 0.85$.

5.2 Modeling Approaches: STD, NEW, and SIM

Fluidization of nearly spherical and uniform density particles, like glass beads, is well-characterized. Fluidization of biomass particles, however, is not as easy to characterize due to the irregular shape and non-uniform density of the particles. Gavi et al. [36] performed a study using FLUENT to computationally validate experimental data of a walnut shell fluidized bed. The experimental setup of the walnut shell fluidized bed can be seen in Franka et al. [37]. The bed has an internal diameter of 15.2 cm and an initial bed height of 15.2 cm. In this study, Gavi et al. explored two approaches, a standard and a new approach, hereafter referred to as STD and NEW. The STD approach employs the nominal material density of the walnut shell, assuming that the particles are spherical and non-porous and that further adjustments in the parameters need not be made. The solids packing limit is specified as the theoretical packing limit of perfectly spherical particles, equal to 0.63. Because Gavi et al. realized that existing drag models were developed for regularly shaped and uniformly dense particles, it was concluded that additional considerations needed to be made to improve the accuracy of the drag model. Since

high drag and low packing had been experimentally observed, purportedly due to porosity of the biomass material, Gavi et al. used an effective density derived from the experimental bed mass and volume, and a solids packing limit equal to that experimentally observed with glass beads of 0.58. The choice of solids packing limit appears to be an arbitrary decision based on the literature [36]. For initial conditions, the bulk density is calculated from the new effective density and the initial solids packing of 0.55 is specified as slightly lower than the solids packing limit to ease the onset of fluidization. Because the initial solids packing is reduced from the solids packing limit used to calculate the effective density, the initial bed height is increased to introduce the correct amount of mass.

The third and final approach to be considered is referred to as the SIM approach. Battaglia et al. [38], like Gavi et al., defined a new approach to model the walnut shell reactor presented in Franka et al. [37] and used the experimental data provided therein as a basis for comparison. Battaglia et al. performed a study to determine how best to capture pressure drop, minimum fluidization velocity and mean void fraction, simultaneously. In simulating fluidized beds, the distributor plate is often omitted. In experimentation, however, the distributor plate causes agglomeration, or dead zones, of solids phase material in between jets of gas phase [39-40]. The fact that not all of the bed material truly fluidizes causes the pressure drop measured in experiments to fall below the theoretical value of pressure drop based on the total bed mass. The study [38] considered two adjustments in system parameters in order to match the pressure drop experimentally measured: modified void fraction and modified bed height. Altering only the bed height, and subsequently the bed mass, provided the best simulation results which matched with the experiments on all desired criteria. A summary of the bed and material properties for each of the three approaches can be seen in Table 5.1.

Table 5.1 Walnut shell bed properties

Property	STD [36]	NEW [36]	SIM [38]
d_p (cm)	0.055	0.055	0.055
ρ_p (g/cm^3)	1.30	0.986	1.30
$\boldsymbol{e}$ (-)	0.9	0.9	0.9
ψ (-)	0.6	0.6	0.6
ε_g^* (-)	0.56	0.55	0.564
$\varepsilon_{s,max}^*$ (-)	0.63	0.58	0.63
$h_{0\ (cm)}$	15.2	16.5	11.7

Gavi et al. [36] did not show simulation results in the unfluidized bed regime for the STD and NEW approaches. Battaglia et al. [38], however, did show pressure drop data in the unfluidized bed regime for the SIM approach determined using the code MFIX. The purpose of this chapter is find the best possible approach to model the walnut shell bed in the unfluidized and fluidized regimes using FLUENT.

5.3 Void Fraction Results and Discussion

The walnut shell bed modeled in the simulations has an inner diameter of 15.2 cm and a total height of 60 cm. The static bed height varies for each approach. Simulations were run using a time step of 10^{-4} seconds for 35 seconds of flow time with time-averaging taken between 5 and 35 seconds over 30,000 time realizations (every 0.001 seconds) for each of the cases shown in Table 5.1. The inlet gas velocity was specified as 2 U_{mf} or 36.2 cm/s. Figure 5.1 shows localized time-averaged void fraction profiles for each of the approaches and the experiments at varying bed heights normalized with initial static bed height. It is clear from Figure 5.1 that each of the approaches yields results that match the experimental data fairly well. However, the NEW approach shows two distinct peaks at h/h_o = 0.25 and 0.5, which is not consistent with the other

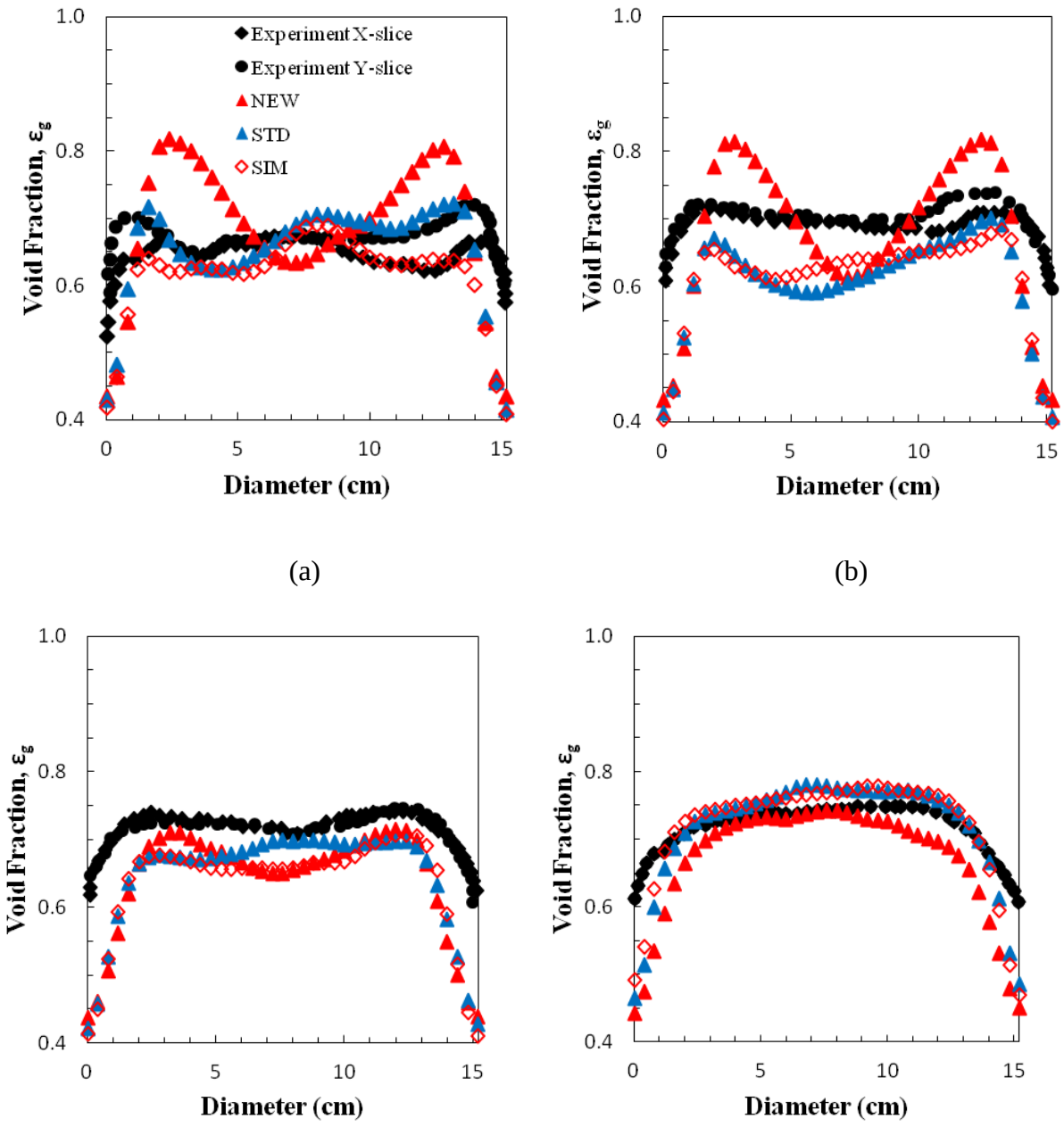

Figure 5.1 Time-averaged void fraction profiles comparing walnut shell bed simulations with experimental data at (a) h/h_0=0.25, (b) h/h_0=0.5, (c) h/h_0=0.75, and (d) h/h_0=1

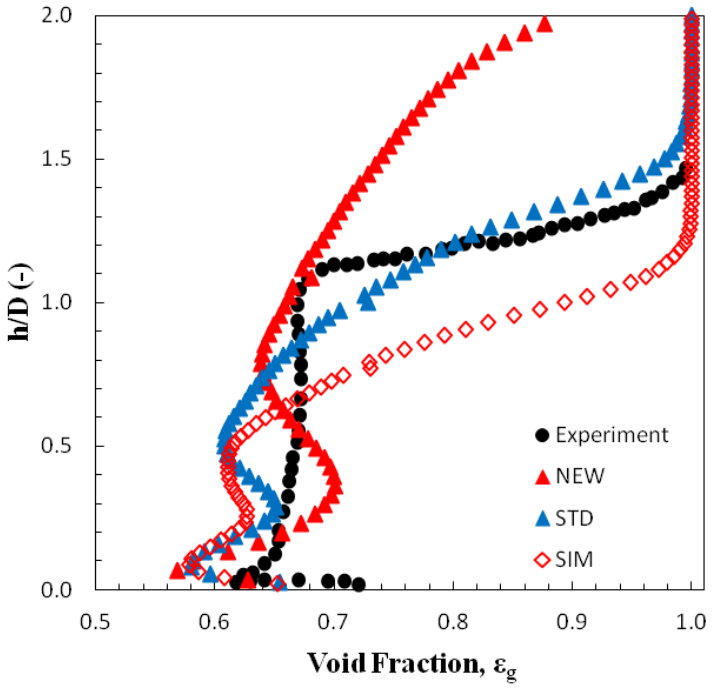

Figure 5.2 Time- and plane-averaged void fraction versus bed height normalized with bed diameter for the walnut shell fluidized bed

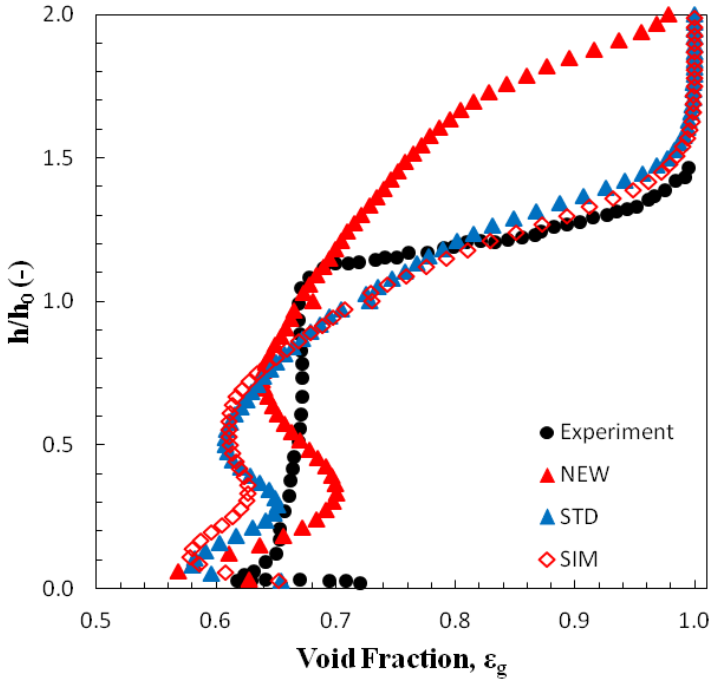

Figure 5.3 Time- and plane-averaged void fraction versus bed height normalized with bed diameter for the walnut shell fluidized bed

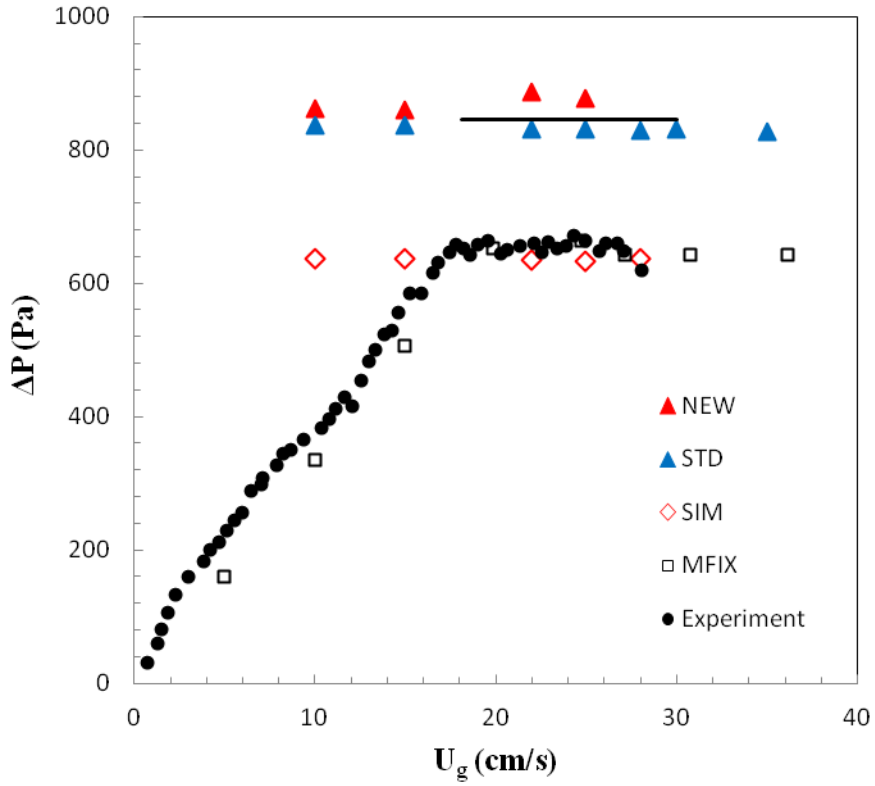

Figure 5.4 Plot of pressure drop versus inlet gas velocity for the walnut shell fluidized bed for simulations having 'Case 1' parameters from Table 5.2

data. The peaks occur because adding mass to the system, as the NEW approach does, creates high regions of void fraction due to bubbles struggling to penetrate the bed. Figure 5.2 presents void fraction in the bed a time- and plane-averaged void fraction versus bed height normalized with the bed diameter. It is not surprising that the STD model matches the experiments the best out of the three approaches when normalized with the bed diameter since it is the only approach that does not adjust the initial bed height. As such, it is more useful to normalize the bed height with the initial static bed height. Figure 5.3 shows time- and plane-averaged void fraction versus bed height normalized with initial static bed height. Figure 5.3 highlights that the STD

Table 5.2 Pressure drop parametric study case parameters

Property	Case 1	Case 2	Case 3	Case 4	Case 5	Case 6
$\varepsilon_{s,max}^{*}$ (-)	0.63	0.63	0.436	0.436	0.63	0.436
frictional viscosity model	Schaeffer	Schaeffer	Schaeffer	Johnson	Schaeffer	Schaeffer
frictional packing limit	0.5	0.5	0.36	0.36	0.5	0.36
drag model	Gidaspow	Gidaspow	Gidaspow	Gidaspow	Syamlal	Syamlal
packed bed model	No	Yes	No	No	No	No
10cm/s ΔP (Pa)	636	94	636	605	634	638
15cm/s ΔP (Pa)	637	131	636	636	658	635

approaches and SIM approaches match the experimentally measured void fraction fairly well, and that the NEW approach over-predicts the bed expansion due to the effective density and increased height incorporated in the approach.

5.4 Pressure Drop Results and Discussion

Many times in reported studies, only the fluidized regime of the bed is simulated. Another important consideration when modeling fluidized beds is the prediction of pressure drop in the unfluidized regime. The contrast between the increasing trend in pressure drop in the unfluidized regime and the near constant value the pressure drop assumes in the fluidized regime allows for the minimum fluidization velocity to be identified (see Figure 2.3). Figure 5.4 shows a plot of pressure drop across the bed versus inlet gas velocity for each of the three approaches, the experimental data [37], and the MFIX simulation data [38]. Data points are shown for several inlet gas velocities in the unfluidized and fluidized regimes. It is clear from Figure 5.4 that the SIM approach is the only approach that correctly predicts the pressure drop in the fluidized regime. The STD and NEW approaches greatly over-predict the pressure drop. For pressure drop values corresponding to inlet gas velocities of 10 cm/s and 15 cm/s (unfluidized regime), however, none of the three approaches correctly predict the linearly increasing trend. A parametric study, as outlined in Table 5.2, was performed for the inlet gas velocities in the

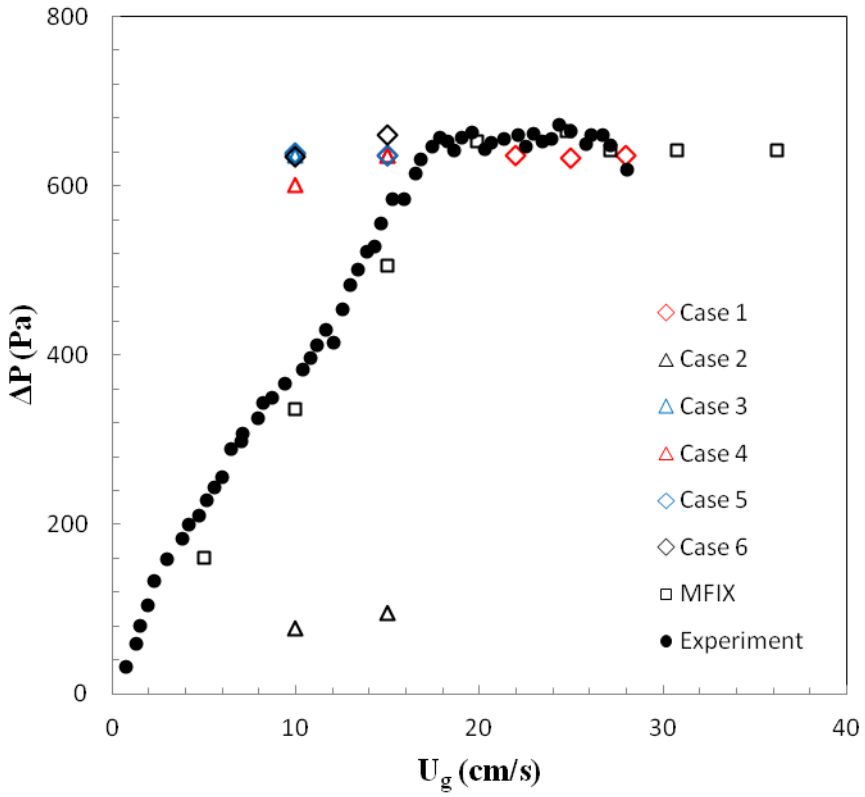

Figure 5.5 Plot of pressure drop versus inlet gas velocity for the walnut shell fluidized bed of the SIM approach parametric study.

unfluidized regime for the SIM approach. Only the SIM approach was chosen for its reliability in void fraction and fluidized bed pressure drop predictions. Key parameters thought to play a potential role in pressure drop values in the unfluidized regime were solids packing limit, frictional viscosity model and frictional packing limit, drag model, and the packed bed model Frictional viscosity plays a major role in the bed's plastic regime where momentum exchange occurs mainly from particles rubbing against each other, as might be expected in a low inlet gas velocity flow. The packed bed model is used to inhibit the granular bed from expanding vertically. The simulations corresponding to the data shown in Figure 5.4 used the parameters corresponding to Case 1 in Table 5.2.

Figure 5.5 shows the plot of pressure drop versus inlet gas velocity for each of the cases shown in Table 5.2. The most obvious conclusion to draw from a first glance of Figure 5.5 is that none of the cases in the parametric study capture the correct pressure drop in the unfluidized regime, however, there is valuable information to be drawn from the plot. It is clear that the addition of the packed bed model from Case 1 to Case 2 reduces the pressure drop to almost negligible values. The addition of the packed bed model requires a lower time step ($\sim 10^{-6}$ seconds) to meet convergence criteria and takes approximately three times longer to run than cases without the packed bed model. Physically, this makes sense since the packed bed model is designed to inhibit motion of the granular bed as previously stated. Cases 3-4 and 6 alter the solids packing limit, making it equivalent to the initial solids volume fraction. The frictional packing limit should be specified as a value lower than the solids packing limit in order for the model to have an effect on the bed dynamics. Therefore, in the cases where the solids packing limit is altered, the frictional packing limit is also altered. Case 4 also uses the Johnson frictional viscosity model as opposed to the Schaeffer model. Case 5 uses the Syamlal-O'Brien drag model as opposed to the Gidaspow model, but keeps the theoretical value of solids packing limit for spherical particles. Case 6 also uses the Syamlal-O'Brien drag model, but uses the altered value of solids packing limit as previously mentioned. Figure 5.5 reveals that none of these adjustments to the simulation case setup have any substantial effect on pressure drop in the unfluidized regime.

It is the conclusion of this chapter that the SIM approach is the best approach for modeling fluidized beds operating in the fluidized regime based on experimental agreement of void fraction and pressure drop data. Also, it can be concluded that FLUENT does not capture the complex physics of a densely packed bed as is characteristic of the unfluidized regime.

Chapter 6 Flow Regime Characterization

Knowing how to characterize in which flow regime a fluidized bed is operating is very important for efficient performance. The following chapter will discuss a method for identifying when a fluidized bed is operating in the bubbling, slugging, or turbulent regime.

6.1 Pressure Fluctuation Analysis

Pressure fluctuation data can be used as a tool to non-invasively predict the operating flow regime and corresponding hydrodynamics of a fluidized bed. Pressure fluctuations are dominated by bubble behavior throughout the bed and originate from two sources: local fluctuations traveling in gas bubbles and fast traveling pressure waves due to bubbles forming, coalescing, and erupting [41-42].

6.1.1 Standard Deviation

Standard deviation of pressure drop, in particular, is used to identify different flow regimes. Standard deviation, σ, of pressure can be calculated by:

$$\sigma = \sqrt{\frac{1}{N-1}\sum_{i=1}^{N}(p_i - \bar{p})^2} \qquad 6.1$$

where N is the number of time realizations, p_i is the pressure drop at each point in the time series ($i = 1,2,\ldots,N$), and $\bar{p}$ is the time-averaged pressure drop for the time interval examined. Figure 6.1 shows a plot of standard deviation versus inlet gas velocity highlighting the zones for bubbling, slugging, turbulent, and fast fluidization regimes. U_c represents the inlet gas velocity where the standard deviation is at a maximum value and also where the flow regime transitions between bubbling and turbulent. The transitional maximum value of standard deviation also

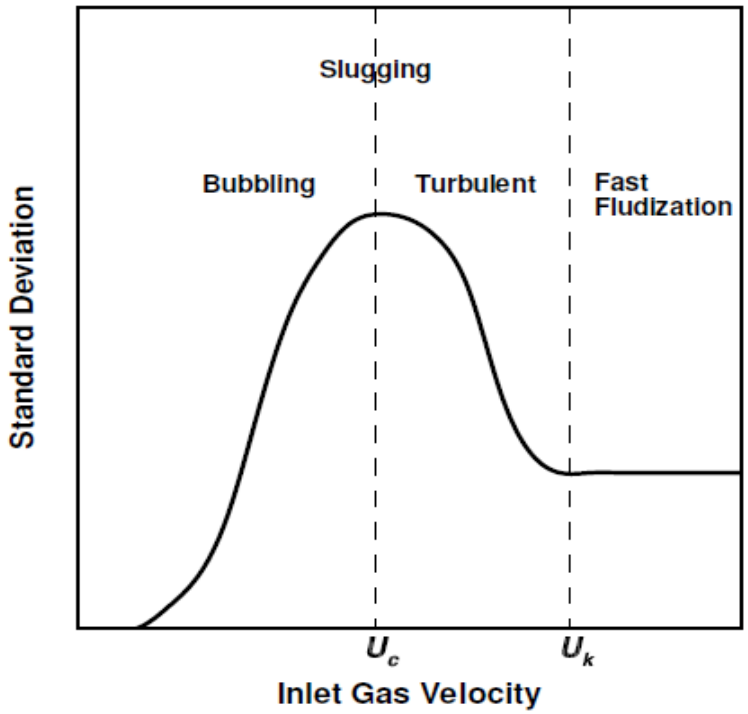

Figure 6.1 Flow regime characterization based on plot of standard deviation versus inlet gas velocity [Image reprinted with permission (Deza 2012)]

corresponds to the slugging regime. U_k denotes the transition from the turbulent to fast fluidization regime, at which point the standard deviation remains essentially constant.

Analysis of pressure fluctuation is widely available based on experimental data since pressure drop calculations are so easily and economically attained [41-44]. Zhang et al. [43-44] observe standard deviations following the same trend as that predicted by Figure 6.1.

6.1.2 Frequency Analysis

An alternative method for analyzing pressure data is frequency analysis achieved by taking a Fourier transform (FFT) and known as power spectral density (PSD) [45-49]. PSD aims to identify dominant frequencies in the pressure time-series and to attribute these dominant

frequencies to physical phenomena occurring in the bed [45]. Kage et al. [45] performed PSD analysis of a gas-solid fluidized bed and obtained three dominant frequencies which corresponded to bubble eruption, bubble generation, and natural frequency of the bed, respectively. Parise et al. [48] used PSD to detect minimum fluidization velocity, or the onset of bed defluidization, in a gas-solid fluidized bed. Frequency analysis can either be expressed by PSD plots (intensity) or Bode plots. Bode plot analysis has revealed that gas-solid fluidized beds behave like second-order mechanical systems [46-47, 49]. Van Ommen et al. [49] showed that Bode plots can be used to identify certain occurrences in fluidization such as single bubbles, multiple bubbles, exploding bubbles, and transport conditions [49].

6.2 Turbulence Modeling

Various simulations discussed in this chapter will include the $k-\epsilon$ mixture turbulence model [27]. A turbulence model is used in order to describe the effects of turbulent fluctuations on velocities and other scalar flow quantities. The mixture model is an extension of the single-phase $k-\epsilon$ turbulence model, and is applicable when phases are separable or stratified to each phase. The k and ϵ equations describing this model are as follows:

$$\frac{\partial}{\partial t}(\rho_m k) + \nabla \cdot (\rho_m \vec{v}_m k) = \nabla \cdot \left(\frac{\mu_{t,m}}{\sigma_k}\nabla k\right) + G_{k,m} - \rho_m \epsilon \qquad 6.2$$

and

$$\frac{\partial}{\partial t}(\rho_m \epsilon) + \nabla \cdot (\rho_m \vec{v}_m \epsilon) = \nabla \cdot \left(\frac{\mu_{t,m}}{\sigma_\epsilon}\nabla \epsilon\right) + \frac{\epsilon}{k}\left(C_{1\epsilon}G_{k,m} - C_{2\epsilon}\rho_m \epsilon\right) \qquad 6.3$$

where the mixture density and velocity, ρ_m and $\vec{v}_m$, are computed from

$$\rho_m = \sum_{i=1}^{N} \varepsilon_i \rho_i \qquad 6.4$$

and

$$\vec{v}_m = \frac{\sum_{i=1}^{N} \varepsilon_i \rho_i \vec{v}_i}{\sum_{i=1}^{N} \varepsilon_i \rho_i} \quad 6.5$$

the turbulent viscosity, $\mu_{t,m}$, is computed from

$$\mu_{t,m} = \rho_m C_\mu \left(\frac{k^2}{\epsilon}\right) \quad 6.6$$

and the production of turbulence kinetic energy, $G_{k,m}$, is computed from

$$G_{k,m} = \mu_{t,m}(\nabla \vec{v}_m + (\nabla \vec{v}_m)^T) : \nabla \vec{v}_m \quad 6.7$$

The model constants have the following defaults values:

$$C_{1\epsilon} = 1.44, C_{2\epsilon} = 1.92, C_\mu = 0.09, \sigma_k = 1.0, \sigma_\epsilon = 1.3$$

which have been determined from experiments with air and water for fundamental turbulent shear flows and have been found to work fairly well for a wide range of wall-bounded and free shear flows [27].

6.3 Problem Setup

The fluidized bed apparatus geometry for the simulations detailed in the present chapter is the same as that shown in Figure 4.1 having an inner diameter of 9.5 cm and an initial static bed height of 10 cm. The bed material is glass beads, and similarly has the same property values as those listed in Table 4.1. Simulations were run for the glass bead fluidized bed with and without a turbulence model for inlet gas velocities ranging from 2 U_{mf} to 9 U_{mf}, where the U_{mf} equals 19.9 cm/s.

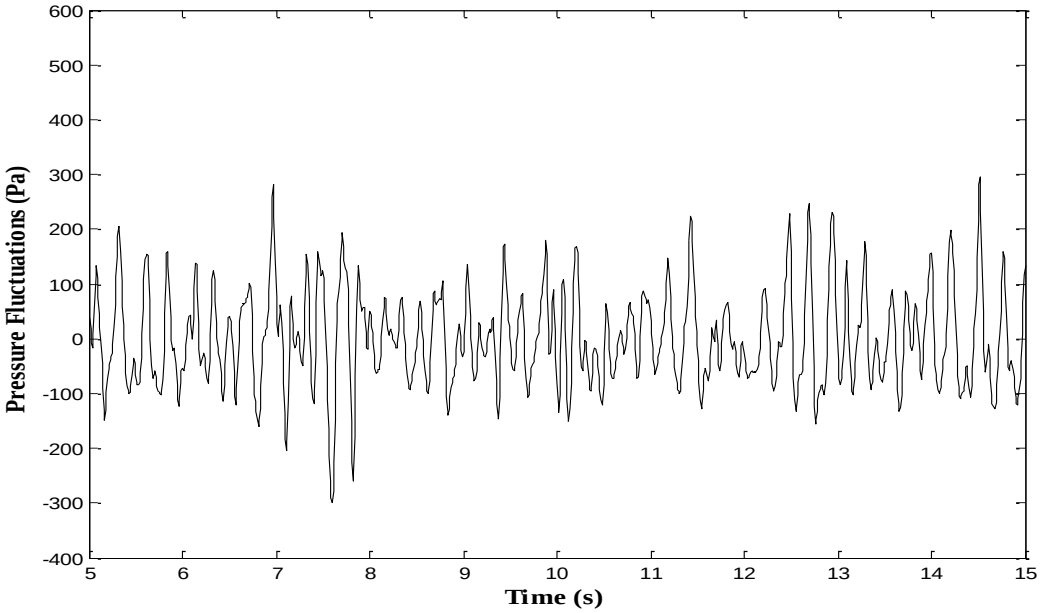

(a)

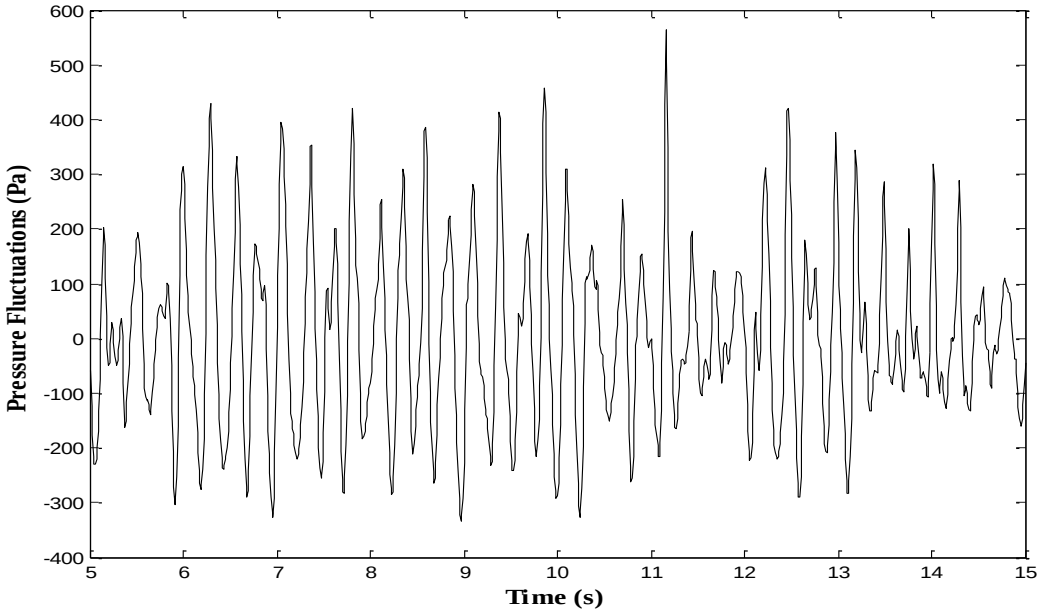

(b)

Figure 6.2 Pressure fluctuations vs. flow time for the glass bead fluidized bed operating at an inlet gas velocity of 2 U_{mf} for (a) no turbulence model and (b) k-epsilon turbulence model

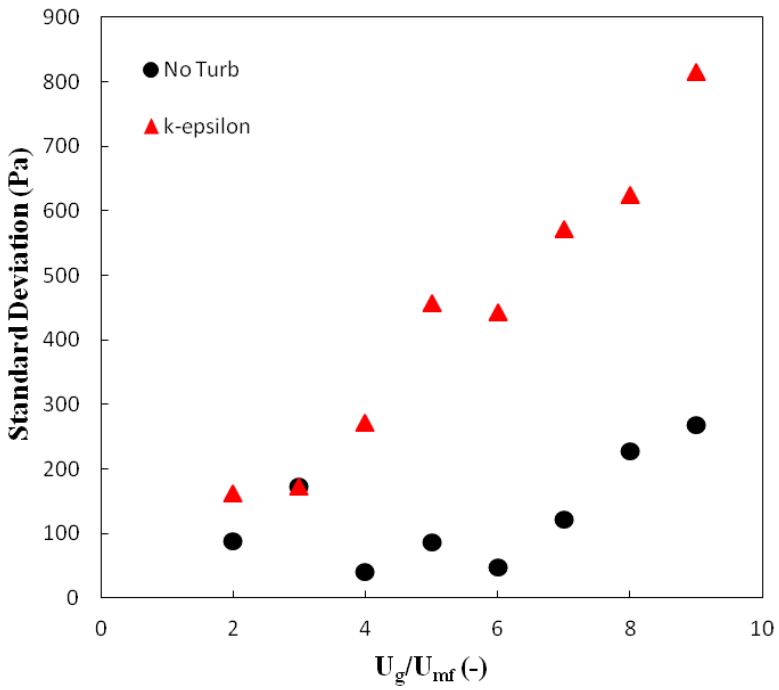

Figure 6.3 Standard deviation of pressure versus inlet gas velocity for simulations with and without a turbulence model

6.4 Numerical Results and Discussion

Simulations for the flow regime study were run using a time step of 10^{-4} seconds for 15 seconds of flow time with time-averaging taken between 5 and 15 seconds for 1000 time realizations (every 0.01 seconds). Before calculating the standard deviations of pressure drop across the bed it is informative to see how pressure is actually varying with flow time. Figure 6.2 shows pressure fluctuations plotted against flow time corresponding to an inlet gas velocity of 2 U_{mf} for a case with no turbulence model (a) and a case with the $k-\epsilon$ turbulence model (b). It is clear from Figure 6.2 that the turbulence model substantially increases the magnitude of the pressure fluctuations.

Figure 6.3 shows a plot of standard deviation of pressure against inlet gas velocity in an attempt for replicate the trends shown in Figure 6.1 for simulations with and without the

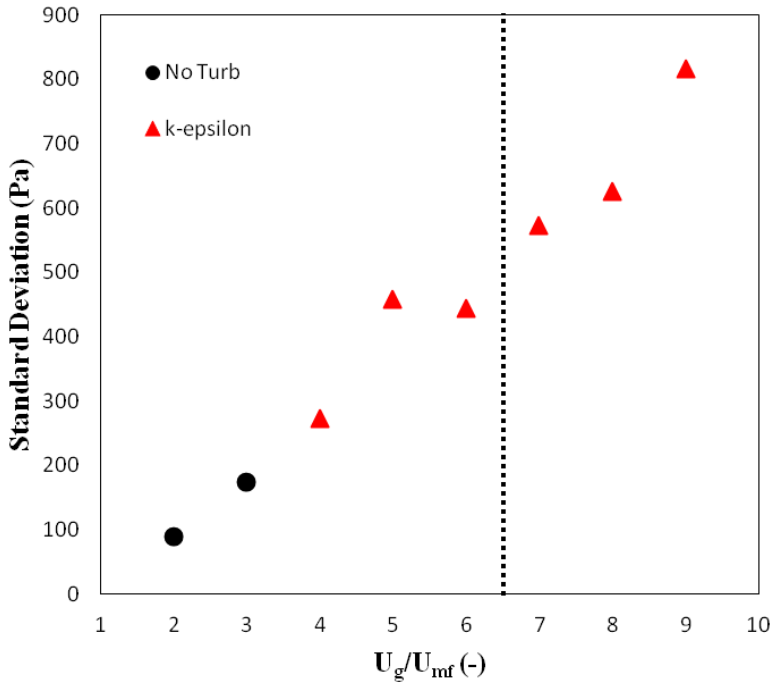

Figure 6.4 Standard deviation of pressure versus inlet gas velocity combining the best results of simulations including and excluding a turbulence model

turbulence model. The standard deviation of the pressure drop for the cases without the turbulence model increase from 2 U_{mf} to 3 U_{mf} as expected, but then deviates from the predicted trend. The addition of turbulence modeling, however, becomes important when the inlet gas velocity reaches around $U_g = 4\ U_{mf}$. As such, it is useful to combine the results of the simulations without turbulence modeling for the lower inlet gas velocity cases (below 3 U_{mf}) with the results of the simulations with turbulence modeling for the higher inlet gas velocity cases (above 4 U_{mf}). Figure 6.4 depicts this combination of results. The resulting plot matches well with the expected trend until an inlet gas velocity of 6 U_{mf}, and afterward the standard deviation continually increases instead of decreasing as expected (see Figure 6.1). The demarcation occurs where the dashed vertical line intersects the plot. The tendency of the

standard deviation to increase in the turbulent regime is attributed to an artifact of modeling in two dimensions as opposed to three dimensions.

The combined plot of standard deviation versus inlet gas velocity (see Figure 6.4) appears to characterize the bubbling and slugging regimes reasonably well, but does not capture the predicted trend in the turbulent regime. It is therefore necessary to peer into contours and bubble behavior in the fluidized regime. Figure 6.5 shows instantaneous time-progressive void fraction contours for the glass bead fluidized bed (no turbulence model) having inlet gas velocities of $3\ U_{mf}$ (top), $5\ U_{mf}$ (middle), and $7\ U_{mf}$ (bottom). The contours corresponding to $3\ U_{mf}$ (bubbling bed) show random bubbling where small bubbles form at the bottom of the bed, coalesce near the top, and erupt calmly at the surface, leaving a fairly level bed surface over time. The contours corresponding to $5\ U_{mf}$ (slugging bed) show the development of larger bubbles that do not have a random pattern, rather where bubbles tend to fall into a single line. The bubbles at the top of the bed consume almost the entire bed diameter, and because the bubbles are larger and take up more space in the bed, the bed expands about 5 cm more than in the bubbling bed. The surface of the bed is no longer level, but remains well-defined. The contours corresponding to the $7\ U_{mf}$ case (turbulent bed) show about another 5 cm increase in bed expansion from the slugging bed. The bubbles are larger, like the slugging bed, only now the bed surface is not clearly defined. Similar to Figure 6.5, Figure 6.6 shows instantaneous time-progressive void fraction contours for the glass bead fluidized bed for the same three inlet gas velocities, only now the simulations include the $k-\epsilon$ turbulence model. The void fraction for $U_g = 3\ U_{mf}$ with the turbulence model shows very large bubbles forming and only moving in the center of the bed. The surface of the bed is curved due to the single rising bubble that erupts at the freeboard, yet is still well-defined. The void fraction for $U_g = 5\ U_{mf}$ with the

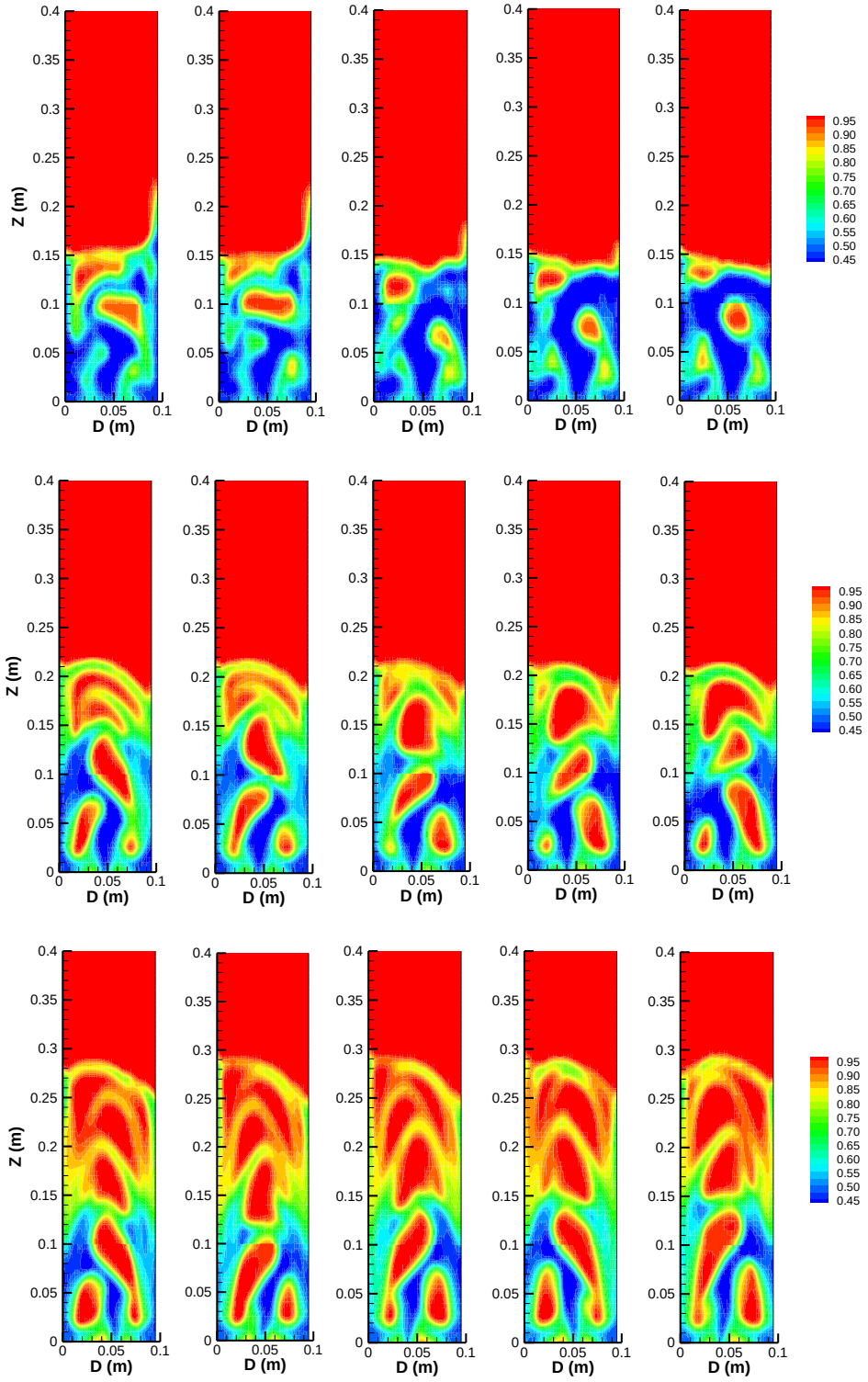

Figure 6.5 Instantaneous void fraction contours of the glass bead fluidized bed without a turbulence model at five sequential flow times for inlet gas velocities of 3 U_{mf} (top), 5 U_{mf} (middle), and 7 U_{mf} (bottom)

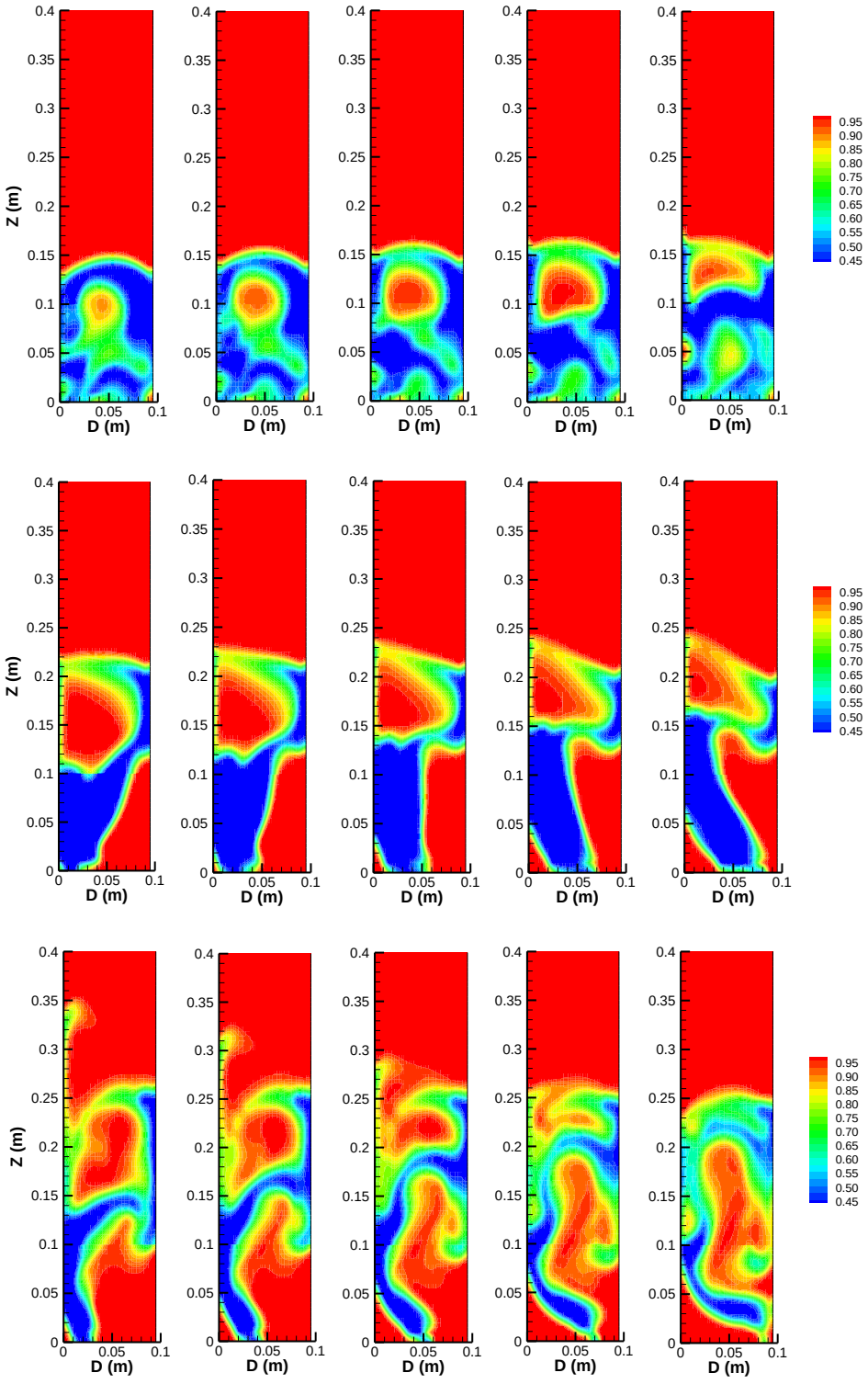

Figure 6.6 Instantaneous void fraction contours of the glass bead fluidized bed with the $k-\epsilon$ turbulence model at five sequential flow times for inlet gas velocities of 3 U_{mf} (top), 5 U_{mf} (middle), and 7 U_{mf} (bottom)

turbulence model predicts a very irregular and nonphysical bed deformation. There is no bubbling, rather the entire bed shifts against the wall. The $U_g = 7\ U_{mf}$ case with the turbulence model, like the slugging bed, shows nonphysical bed behavior where the bed is almost completely lifted from the base of the bed. The turbulent bed does not have a defined bed surface. It is very clear from Figures 6.5 and 6.6 that the simulations without the turbulence model show the most physically accurate bed dynamics. It is important to remember that turbulence is inherently a three-dimensional phenomenon and that trying to capture the physics in a fluidized bed with two-dimensional modeling at high inlet gas velocities may not provide accurate results.

Figure 6.7 shows pairs of time-averaged void fraction contours for the glass bead fluidized bed simulations excluding (left) and including (right) turbulence modeling for inlet gas velocities 3 U_{mf}, 5 U_{mf}, and 7 U_{mf}. Figure 6.8 serves to reiterate the previous acknowledgement that bed dynamics of the simulations with turbulence modeling are nonphysical. Each of the contours of the simulations without turbulence modeling show defined regions of bubble formation at the base of the bed, as well as regions of recirculation and eruption of bed material. The contours corresponding to cases having the turbulence model do not show any real discernible flow features. Therefore, the remaining results will not incorporate a turbulence model.

As previously mentioned, bubble behavior is what causes pressure fluctuations in the bed. Figure 6.8 provides a more in-depth look into bubble dynamics by showing instantaneous void fraction contours and corresponding particle velocity vectors for the glass bead fluidized bed at inlet gas velocities of 3 U_{mf}, 5 U_{mf}, and 7 U_{mf}. The void fraction contours in Figure 6.8(a), for the bubbling bed, show several bubbles which complement the particle velocity vector. The

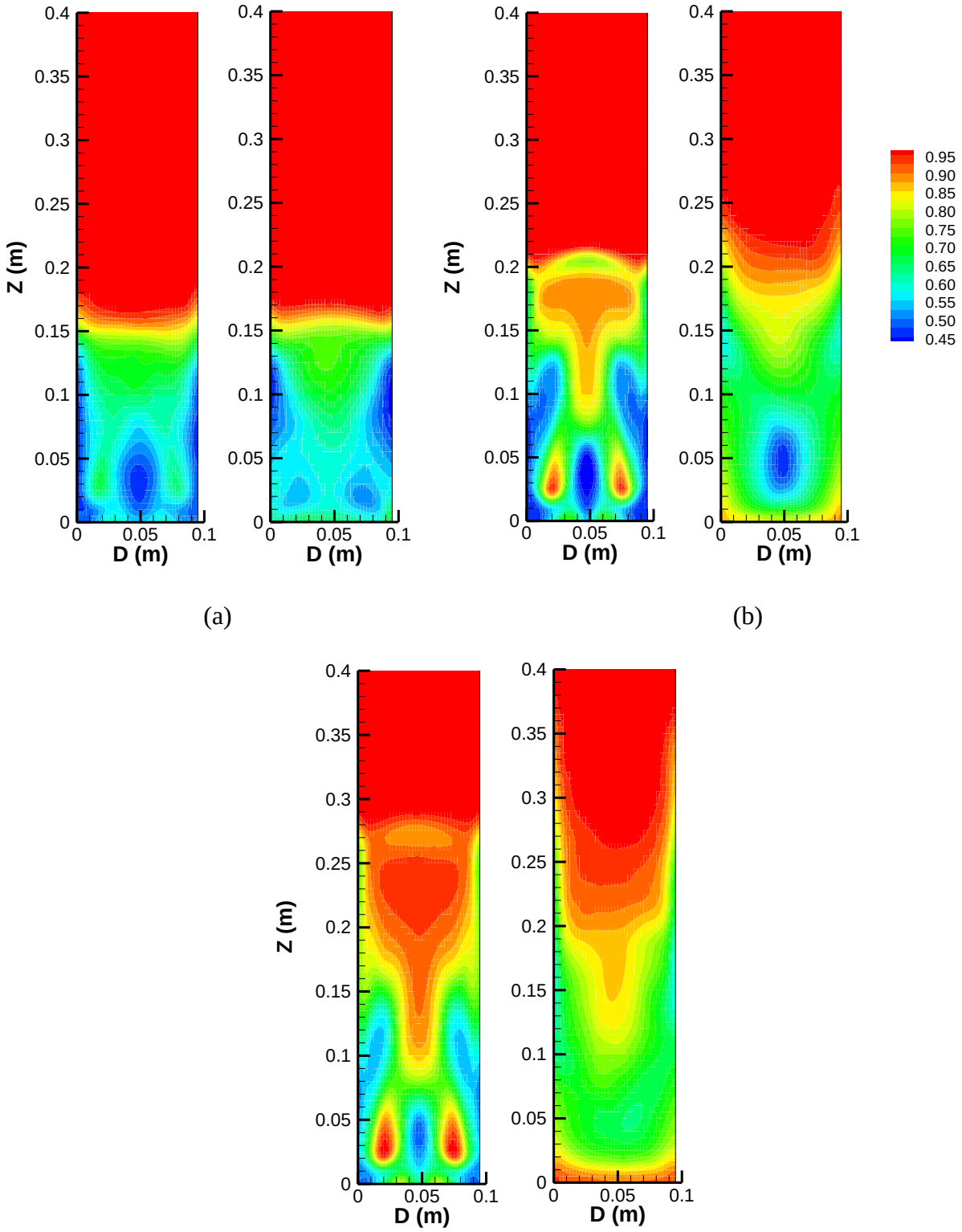

Figure 6.7 Pairs of time-averaged void fraction contours for inlet gas velocities (a) 3 U_{mf}, (b) 5 U_{mf}, and (c) 7 U_{mf} for no turbulence model (left) and $k-\epsilon$ turbulence model (right)

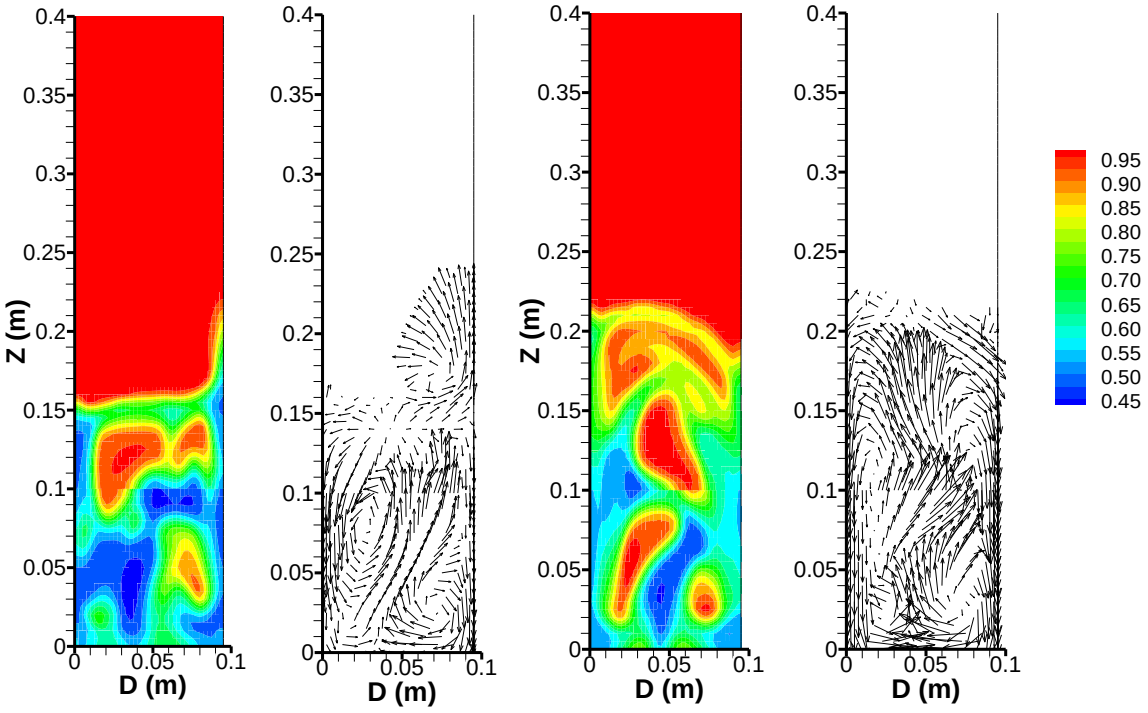

(a) (b)

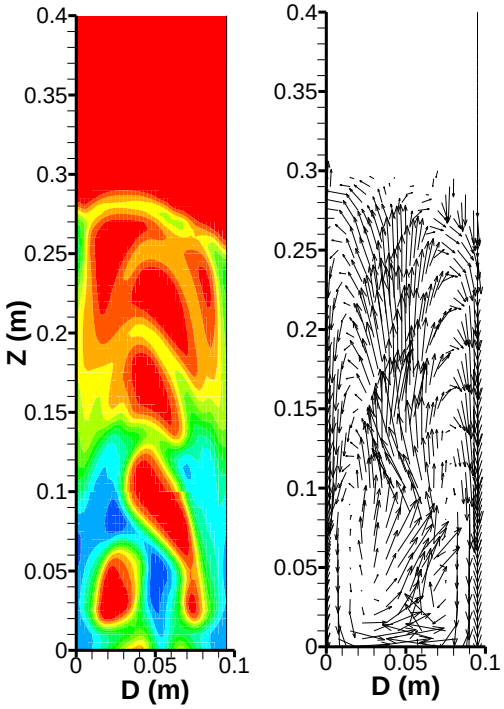

(c)

Figure 6.8 Pairs of instantaneous void fraction (left) and velocity vectors (right) for the glass bead fluidized bed without turbulence modeling for inlet gas velocities (a) 3 U_{mf}, (b) 5 U_{mf}, and (c) 7 U_{mf} at approximately 10 s flow time

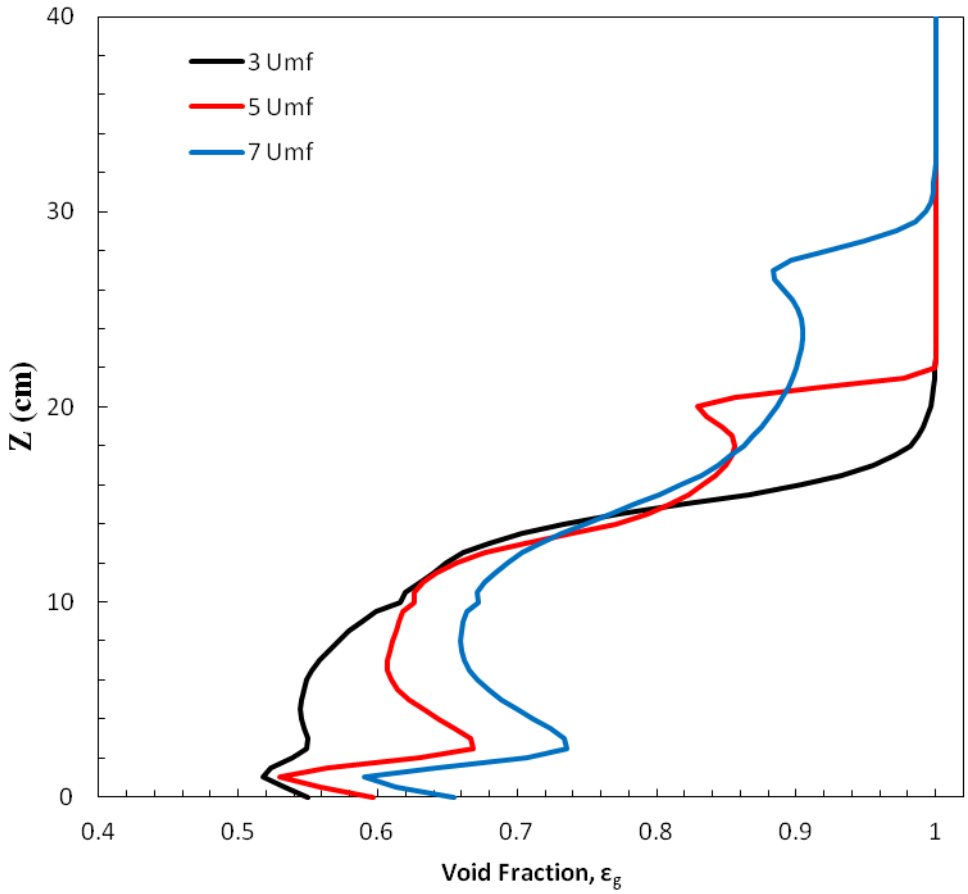

Figure 6.9 Time- and plane-averaged void fraction versus bed height for the glass bead fluidized bed at various inlet gas velocities

bubbles at the bottom of the bed cause the material to move downward along the wall and rise up through the middle. The bubbles at the top are coalescing and increasing in size, so the particle velocity vectors point outward circumferentially from the center of the bubbles. The particle velocity vectors in Figure 6.8(b), for the slugging bed, show that bed material rises through the middle of the bed from the bottom to the surface at which point the material sprays to both sides and falls to re-circulate in the bed. The same two bubble formation and recirculation spots are seen in the bottom of the slugging bed as in the bubbling bed. In Figure 6.8(c), the turbulent bed shows particle velocity vectors having the same tendency as in the slugging bed, where material

erupts from the middle of the bed and falls down both sides, only is more exaggerated. The clear outwardly moving particle velocity vectors exhibited by the bubbling bed are not seen in the slugging and turbulent beds since the bed surfaces of the two latter regimes are not as stable. The base of the bed shows similar behavior to the other two regimes.

Figure 6.9 shows a plot of time- and plane-averaged void fraction versus bed height for the glass bead fluidized bed simulations for inlet gas velocities 3 U_{mf}, 5 U_{mf}, and 7 U_{mf}. It was noted earlier in Figures 6.5 and 6.6 that the bed expansion increases with increasing inlet gas velocity, also lending to the reasoning that void fraction throughout the bed will be higher with increasing inlet gas velocity and can be seen in Figure 6.9. The 5 U_{mf} and 7 U_{mf} cases exhibit a kink near the top of the plot in each of the lines. Referring back to Figure 6.5, this is indicative of the material at the top of the large bubbles near the freeboard.

It can be concluded from the flow regime study that two-dimensional simulations are not sufficient for capturing pressure standard deviation trends in the turbulent regime. It can also be concluded that modeling two-dimensional fluidized beds with the $k - \varepsilon$ turbulence model creates nonphysical flow in appearance, likely due to the fact that turbulence is inherently a three-dimensional phenomenon.

Chapter 7 Conclusions and Future Work

Computational fluid dynamics was used to study the hydrodynamics of gas-solid fluidized beds. An Eulerian multi-fluid model was used to represent the phases as interpenetrating continua and granular kinetic theory was used to model the complex bed dynamics. Specifically, the commercial code ANSYS FLUENT was used to model two-dimensional, single solids phase systems of glass beads and walnut shell. The information presented in this thesis aims to convey an understanding of the complex physics of fluidization as well as to advance understanding of the capabilities of computationally modeling fluidized beds with FLUENT.

It can be concluded that the modeling of glass beads in a fluidized bed is well-characterized due to nearly ideal particle properties and thus served as a good platform to study the basic hydrodynamic properties of fluidized beds. In contrast, Chapter 5 showed that modeling of biomass particles, such as walnut shell, is very difficult due to the shape and porosity of the particles and the fact that current computational codes only allow for spherical and uniform density particles to be modeled. Also, the distributor plate encompassed in experimental setup (but not typically modeled in simulations) causes bed material to agglomerate between jets of gas phase. Due to these dead zones, not all of the bed mass is fluidized, causing experimentally measured pressure drop to fall below theoretical pressure drop based off of the total bed mass. This means that to accurately capture the physics of the biomass fluidized bed, other parameters of the system must be altered. Accordingly, chapter 5 showed that the best modeling approach to capture the physics of the biomass bed was by correcting the amount of mass present in the bed to match the experimentally observed pressure drop whereby the initial bed height of the system is altered. Referred to as the SIM approach, it accurately predicted void

fraction and pressure drop in the fluidized regime. Even the SIM approach, however, could not be shown to correctly predict pressure drop in the unfluidized regime. Accordingly, it can be concluded that FLUENT is not capable of predicting the complex physics in the unfluidized regime, where the bed remains densely packed.

The flow regime study detailed in Chapter 6 showed that standard deviation of pressure only follows the correct trend for identifying the bubbling and slugging flow regimes, not the turbulent regime. This is attributed to an artifact of modeling in two dimensions as opposed to three dimensions. Furthermore, Chapter 6 revealed that simulating two-dimensional beds with the $k-\varepsilon$ turbulence model yields nonphysical bed hydrodynamics. Again, the non-physicality is attributed to an artifact of two-dimensional modeling since it is well understood in the fluids community that turbulence is inherently a three-dimensional phenomenon.

For future work, it would be enlightening to see the pressure drop parametric study of the biomass fluidized bed from Chapter 5 and the flow regime study of Chapter 6 carried out with three-dimensional modeling. Furthermore, since other codes such as MFIX correctly predict the pressure drop in the unfluidized bed regime with two-dimensional modeling, it may be useful as a future project to delve into the codes themselves and identify any discrepancies between the two. Alternatively, the flow regime study could be performed using different turbulence models on the two-dimensional bed. Pressure fluctuation analysis could be represented through frequency plots (Fourier transforms) of the pressure data. In order to have sufficient data for frequency plots, the simulations would need to be run for a minimum of 60 seconds flow time.

Bibliography

[1] Bridgewater, A. V., Meier, D., & Radlein, D. (1999). An Overview of Fast Pyrolysis of Biomass. *Organic Geochemistry, 30*, 1479-1493.

[2] Demirbas, A. (2002). An Overview of Biomas Pyrolysis. *Energy Source, 24*, 471-482.

[3] Gidaspow, D. (1994). *Multiphase Flow and Fluidization: Continuum and Kinetic Theory Descriptions*. Boston, USA: Academic Press.

[4] Cui, H., & Grace, J. R. (2007). Fluidization of Biomass Particles: A Review of Experimental Multiphase Flow Aspects. *Chemical Engineering Science, 62*(1-2), 45-55.

[5] Papadikis, K., Bridgewater, A., & Gub, S. (2008). CFD Modeling of the Fast Pyrolysis of Biomass in Fluidized Bed Reactors, Part A: Eulerian Computuation of Momentum Transport in Bubbling Fluidized Beds. *Chemical Engineering Science, 63*, 4218-4227.

[6] Deza, M. (2012). *Modeling the Hydrodynamics of a Biomass Fluidized Bed.* PhD Dissertation, Virginia Tech, Blacksburg, VA.

[7] Ergun, S. (1952). Fluid Flow through Packed Columns. *Chemical Engineering Progress, 48*(2), 89-94.

[8] Taghipour, F., Ellis, N., & Wong, C. (2005). Experimental and Computational Study of Gas-solid Fluidized Bed Hydrodynamics. *Chemical Engineering Science, 60*(24), 6857-6867.

[9] Syamlal, M., & O'Brien, T. J. (1989). Computer Simulation of Bubbles in a Fluidized Bed. *American Institute of Chemical Engineers Symposium Series, 85*, 22-31.

[10] Wen, C. Y., & Yu, Y. H. (1966). A Generalized Method for Predicting the Minimum Fluidization Velocity. *AlChE, 12*(1), 610-612.

[11] Du, W., Bao, X., Xu, J., & Wei, W. (2006). Computational Fluid Dynamics (CFD) Modeling of Spouted Bed: Assessment of Drag Coefficient Correlations. *Chemical Engineering Science, 61*(5), 1401-1420.

[12] Richardson, J. R., & Zaki, W. N. (1954). Sedimentation and Fluidization: Part I. *Transactions of the Institute of Chemical Engineering, 32*(1), 35-53.

[13] DiFelice, R. (1994). The Voidage Functions for Fluid-Particle Interaction System. *International Journal of Multiphase Flow, 20*(1), 153-159.

[14] Arastoopour, H., Pakdel, P., & Adewumi, M. (1990). Hydrodynamic Analysis of Dilute Gas-Solids Flow in a Vertical Pipe. *Powder Technology, 62*(2), 163-170.

[15] Mahinpey, N., Vejahati, F., & Ellis, N. (2007). *CFD Simulation of Gas-Solid Bubbling FLuidized Bed: An Extensive Assessment of Drag Models.* Paper presented at the 4th International Conference on Computational and Experimental Methods in Multiphase and Complex Flow, Bologna, Italy.

[16] Gibilaro, L. G., DiFelice, R., & Waldram, S. P. (1985). Generalized Friction Factor and Drag Coefficient Correlations for Fluid-Particle Interactions. *Chemical Engineering Science, 40*(10), 1817-1823.

[17] Koch, D. L., & Hill, R. J. (2001). Inertial Effects in Suspension and Porous-Media Flows. *Annual Review of Fluid Mechanics, 33*, 619-647.

[18] Zhang, Y., & Reese, J. M. (2003). The Drag Force in Two Fluid Models of Gas-Solid Flows. *Chemical Engineering Science, 58*(8), 1641-1644.

[19] Deza, M., Franka, N. P., Heindel, T. J., & Battaglia, F. (2009). CFD Modeling and X-ray Imaging of Biomass in a Fluidized Bed. *Journal of Fluids Engineering, 131*(11).

[20] Geldart, D. (1973). Types of Gas Fluidization. *Powder Technology, 7*(5), 285-292.

[21] Bi, H. T., Grace, J. R., & Lim, K. S. (1995). Transition from Bubbling to Turbulent Fluidization. *Industrial and Engineering Chemistry Research, 34*, 4003-4008.

[22] Bi, H. T., Grace, J. R., & Zhu, J. X. (1995). Regime Transitions Affecting Gas-solid Suspensions in Fluidized Beds. *Transactions of the Institution of Chemical Engineers, 73*, 154-161.

[23] Hulme, I., Clavelle, E., Lee, L. v. d., & Kantzas, A. (2005). CFD Modeling and Validation of Bubble Properties for a Bubbling Fluidized Bed. *Industrial and Engineering Chemistry Research, 44*, 4254-4266.

[24] Benyahia, S., Arastoopour, H., Knowlton, T. M., & Massah, H. (2000). Simulation of Particles and Gas Flow Behavior in the Riser Section of a Circulating Fluidized Bed using the Kinetic Theory Approach for the Particulate Phase. *Powder Technology, 112*, 24-33.

[25] Sahoo, A., Ramesh, C., & Biswal, K. C. (2009). Experimental and Computational Study of the Bed Dynamics of Semi-Cylindrical Gas-Solid Fluidized Bed. *The Canadian Journal of Chemical Engineering, 87*, 11-18.

[26] Herzog, N., Schreiber, M., Egbers, C., & Krautz, H. J. (2012). A Comparative Study of Different CFD-Codes for Numerical Simulation of Gas-Solid Fluidized Bed Hydrodynamics. *Computers and Chemical Engineering, 39*, 41-46.

[27] ANSYS-INC. (2009). Theory Guide: ANSYS FLUENT 12.0.

[28] ANSYS-INC. (2010). User's Guide: ANSYS FLUENT 13.0.

[29] Rowe, P. N. (1961). Drag Forces in a Hydraulic Model of Fluidized Bed - Part II. *Transactions of the Institute of Chemical Engineering, 39*, 175-180.

[30] Lun, C. K. K., Savage, S. B., & Jeffrey, D. J. (1984). Kinetic Theories for Granular Flow - Inelastic Particles in Coutte-Flow and Slightly Inelastic Particles in a General Flowfield. *Journal of Fluid Mechanics, 140*(MAR), 223-256.

[31] Patankar, S. V. (1980). *Numerical Heat Transfer and Fluid Flow*. Washington: Hemisphere Publishing Corporation.

[32] Leonard, B. P. (1979). A Stable and Accurate Convective Modeling Procedure Based on Quadratic Upstream Interpolation. *Computational Methods in Applied Mechanics and Engineering, 19*, 59-98.

[33] Franka, N. P., Heindel, T. J., & Battaglia, F. (2008). *Visualizing Cold-flow Fluidized Beds with X-rays*. Paper presented at the Proceedings of the 2007 ASME International Mechanical Engineering Congress and Exposition, New York, NY.

[34] Heindel, T. J., Gray, J. N., & Jensen, T. C. (2008). An X-ray System for Visualizing Fluid Flows. *Flow Measurement and Instrumentation, 9*(2), 67-78.

[35] Heindel, T. J., Hubers, J. L., Jensen, T. C., Gray, J. N., & Striegel, A. C. (2005). *Using X-rays for Multiphase Flow Visualization*. Paper presented at the Proceedings of the 2005 ASME Fluids Engineering Division Summer Conference, New York, NY.

[36] Gavi, E., Heindel, T. J., & Fox, R. O. (2010). *Modeling Fluidization in Biomass Gasification Processes*. Paper presented at the International Conference of Multiphase Flow, Tampa, FL.

[37] Franka, N. P., Drake, J., & Heindel, T. J. (2008). *Minimum Fluidization Velocity and Gas Holdup in Fluidized Beds with Side Port Air Injection*. Paper presented at the Proceedings of the 2008 ASME Fluids Engineering Division Summer Conference.

[38] Battaglia, F., England, J. A., Kanholy, S., & Deza, M. (2010). *On the Modeling of Gas-solid Fluidization: Which Physics are Most Important to Capture?* Paper presented at the Proceedings of the 2010 ASME International Mechanical Engineering Congress and Exposition, Vancouver, British Columbia.

[39] Agarwal, G., Lattimer, B., Ekkad, S., & Vandsburger, U. (2011). Influence of Multiple Gas Inlet Jets on Fluidized Bed Hydrodynamics using Particle Image Velocimetry and Digital Image Analysis. *Powder Technology, 214*, 122-134.

[40] van Ommen, J. R., Schouten, J. C., & van den Bleek, C. M. (1999). Monitoring Fluidization Dynamics for Detection of Changes in Fluidized Bed Composition and Operating Conditions. *Journal of Fluids Engineering, 121*, 887-894.

[41] Puncochar, M., & Drahos, J. (2005). Origin of Pressure Fluctuations in Fluidized Beds. *Chemical Engineering Science, 60,* 1193-1197.

[42] Sobrino, C., Sanchez-Delgado, S., Garcia-Hernando, N., & deVega, M. (2008). Standard Deviation of Absolute and Differential Pressure Fluctuations in Fluidized Beds of Group B Particles. *Chemical Engineering Research and Design, 86*(11A), 1236-1242.

[43] Zhang, Y., Jin, B., & Zhong, W. (2008). Fluidization, Mixing, and Segregation of Biomass-Sand Mixture in a Fluidized Bed. *International Journal of Chemical Engineering Reactor, 6*(A88).

[44] Zhang, Y., Jin, B., Zhong, W., Ren, B., & Xiao, R. (2009). Characterization of Fluidization and Segregation of Biomass Particles by Combining Image Processing and Pressure Fluctuation Analysis. *International Journal of Chemical Engineering Reactor, 7*(A81).

[45] Kage, H., Iwasaki, N., Yamaguchi, H., & Matsuno, Y. (1991). Frequency Analysis of Pressure Fluctuations in Fluidized Bed Plenum. *Journal of Chemical Engineering of Japan, 24*(1), 76-81.

[46] Brue, E., & Brown, R. C. (2001). Resolving Dynamical Features of Fluidized Beds from Pressure Fluctuations. *Powder Technology, 119*(2-3), 68-80.

[47] Brue, E., & Brown, R. C. (2001). Use of Pressure Fluctuations to Validate Hydrodynamic Similitude in Fluidized Media: Bubbling Beds. *Powder Technology, 119*(2-3), 117-127.

[48] Parise, M. R., Kurka, P. R. G., & Taranto, O. P. (2009). The Gaussian Spectral Pressure Distribution Applied to a Fluidized Bed. *Chemical Engineering and Processing: Process Intensification, 48,* 120-125.

[49] van Ommen, J. R., Sasic, S., van der Schaaf, J., Gheorghiu, S., Johnsson, F., & Coppens, M. O. (2011). Time-Series Analysis of Pressure Fluctuations in Gas-Solid Fluidized Beds - A Review. *International Journal of Multiphase Flow, 37,* 403-428.